Plume–Lithosphere Interaction during Migration of Cretaceous Alkaline Magmatism in Southwest Portugal: Evidence from U–Pb ages and Pb–Sr–Hf isotopes.

M. GRANGE[1,*], U. SCHARER[1], R. MERLE[2], J. GIRARDEAU[3], AND G. CORNEN[3]

[1] UNIVERSITE DE NICE - SOPHIA ANTIPOLIS, GEOAZUR (UMR 6526), PARC VALROSE, F-06108 NICE, FRANCE.

[2] UNIVERSITY OF WESTERN AUSTRALIA, SCHOOL OF EARTH AND ENVIRONMENT, 35 STIRLING HIGHWAY, CRAWLEY WA 6009, AUSTRALIA

[3] UNIVERSITE DE NANTES, LABORATOIRE DE PLANETOLOGIE ET GEODYNAMIQUE (UMR 6112), 2 RUE DE LA HOUSSINIERE, F-44322 NANTES CEDEX 3, FRANCE.

* Corresponding author. Present address: Department of Applied Geology, Curtin University of Technology, Level 2, building 312, GPO Box U1987, Perth, WA 6845, Australia.

Tel: +61 8 9266 7969. Fax: +61 8 9266 3153. E-mail: m.grange@curtin.edu.au

ABSTRACT

Large massifs of alkaline rocks are exposed along about 250 km of the Atlantic coast of Portugal. Their origin is still poorly understood, including the precise timing of their emplacement and their relationships with the well-constrained alkaline magmatic rocks that occur 200–1000 km offshore. To elucidate the precise timing and origin of the alkaline magmatism in this region, magmatic rocks from the three major alkaline massifs of Portugal (Sintra, Sines, and Monchique) and an isolated diorite intrusion (Ribamar, north of Sintra) have been dated by the U–Pb method on titanite and zircon and characterized using Pb, Sr, and Hf isotopic compositions obtained on feldspar and zircon. From north to south, the resulting ages are: 88.3 ± 0.5 Ma (95% conf. level) for Ribamar, 83.4 ± 0.7, 82.0 ± 0.7, 81.7 ± 0.4, and 80.1 ± 1.0 Ma for the Sintra complex, 77.2 ± 0.6, 77.2 ± 0.4, and 76.1 ± 1.3 Ma for the Sines massif, and 70.0 ± 2.9 Ma and 68.8 ± 1.0 for the Monchique complex. Initial isotopic compositions of Pb in feldspars lie at 18.522–19.299 for $^{206}Pb/^{204}Pb$, 15.555–16.007 for $^{207}Pb/^{204}Pb$, and 38.480–39.330 for $^{208}Pb/^{204}Pb$. Initial $^{87}Sr/^{86}Sr$ of feldspars range between 0.70274 and 0.70481 and initial Hf isotope ratios yield εHf_i between +3.7 and +9.6.

These results, together with major, trace, and rare earth element analyses, show that the ages, the $(^{207}Pb/^{204}Pb)_i$, and the $(^{87}Sr/^{86}Sr)_i$ increase northward, whereas the alkaline affinity, the $(^{206}Pb/^{204}Pb)_i$, and the εHf_i increase southward, substantiating a N–S pattern of geochemical and age variation. The isotopic composition of the studied rocks can be explained by a two-component source, composed of a sub-lithospheric mantle source with an enriched DMM (Depleted MORB Mantle) signature and contaminated by the metasomatized Iberian subcontinental lithospheric mantle (SCLM). The N–S age trend is in agreement with the motion of the Iberian plate between 88 and 60 Ma. The spatial and temporal variations of the isotopic signatures are explained by differences in the contribution of the two components involved in the source. The sub-lithospheric mantle-derived magmas are more contaminated by

the SCLM in the northern part of the alignment, and therefore have a signature closer to the SCLM fingerprint, as compared to the southern part of the studied region, where the rocks have isotopic signatures closer to the enriched sub-lithospheric mantle.

Our data are further incorporated into a geodynamical model that explains the overall distribution of alkaline magmatism in this part of the Atlantic region, and provides new constraints of the occurrence of alkaline magmatism along the Iberian margin and in the north–west African plate. The spatial distribution of these rocks is directly correlated with the motion of Iberian plate above a deep-rooted thermal anomaly. These alkaline rocks originate from a sub-lithospheric source driven by a mantle plume that has emitted magmatic pulses since the Cretaceous.

KEY-WORDS: alkaline magmatism, U–Pb geochronology, Pb–Sr–Hf isotope, subcontinental lithospheric mantle (SCLM), Portugal.

INTRODUCTION

Recent geochronological and isotopic investigations suggest that a plume-related thermal anomaly below the eastern North Atlantic region has been the cause of widespread alkaline magmatic activity since the Cretaceous (e.g., Geldmacher *et al.*, 2006; Merle *et al.*, 2006; 2009). These manifestations occur in the oceanic region west of North Africa and Iberia (Fig. 1), along the SW–NE trending Tore-Madeira rise (TMR), which comprises a dozen seamounts from the Madeira Archipelago to the submarine Tore seamounts, on the Gorringe Bank in the vicinity of the Azores-Gibraltar fracture zone (AGFZ), 200 km SE of Portugal, and on two off-centred seamounts between the Gorringe Bank and the Madeira Archipelago (namely Ampere and Coral-Patch seamounts).

On the continent, alkaline magmatic rocks are also present along the Iberian margin in Portugal, occurring as three main massifs and several isolated sills and plugs. However, a lack of age and isotopic constraints makes it difficult to establish reliable petrogenetic relationships between the continental and the oceanic alkaline magmatism, despite models that suggest the southernmost massif of Portugal (Monchique) and the eastern part of the Gorringe Bank (Mount Ormonde) were emplaced at the same time and originated from similar sources (Cornen, 1982; Bernard-Griffiths *et al.*, 1997). A recent study has also shown that the alkaline magmatism in this region (i.e., along the TMR, on the seamounts between TMR and along the coast of the Portugal) can be geodynamically explained by the movement of the Iberian plate above a thermal anomaly emitting magmatic pulses since the Cretaceous (Merle *et al.*, 2009).

In this paper, we investigate the precise timing of emplacement of the Portugal massifs using U–Pb dating on zircon and titanite by ID-TIMS methods. We also trace their magma sources using Pb–Sr and Hf isotope systematics on feldspar and zircon, and major and trace element analyses on whole rock samples. The present study therefore addresses the questions of (i) the temporal and spatial extent of alkaline magmatism in Portugal, (ii) the magma

sources, including the possible involvement and interaction of both plume- and subcontinental lithospheric mantle (SCLM)-derived magmas, and (iii) the relationships between the continental and oceanic alkaline magmatism in the context of eastern North Atlantic geodynamics.

GEOLOGICAL FRAMEWORK

General setting

The western Iberian margin was structurated during the Cretaceous when the Iberian microplate separated from Newfoundland. The 130–125 Ma magnetic anomaly (J-anomaly) was the first magnetic anomaly formed by the Mid-Atlantic Ridge north of the AGFZ and marks the western limit of the continent–ocean transition zone on the Iberia margin (Olivet, 1996). The continent–ocean transition is characterised by the unroofing of the subcontinental lithospheric mantle made up of serpentinised peridotites locally covered by thin sediment deposits (e.g., Boillot *et al.*, 1988; Beslier *et al.*, 1990; Girardeau *et al.*, 1998). Moreover, previous studies have shown that the Gorringe Bank is also a piece of unroofed SCLM, tilted during the North Atlantic rifting and later capped by Cretaceous–Palaeocene alkaline magmatic rocks (e.g., Féraud *et al.*, 1986; Girardeau *et al.*, 1998; Schärer *et al.*, 2000). The SCLM of the western Iberian margin may be very heterogeneous due to Variscan orogenesis (400-250 Ma). During this orogenic cycle, the margin experienced subduction and associated mantle metasomatism, and the accretion of allochtonous terranes such as the Cabo Ortegal complex, which is a piece of metamorphosed and exhumed island arc (Girardeau & Gil Ibarguchi, 1991; Santos *et al.*, 1996; 2002).

The AGFZ is a major oceanic transform fault that constitutes the boundary between the African plate to the south and the European plate to the north since about 85 Ma, and formed in

response to the northward motion of Africa (Sibuet *et al.*, 2004). Although this fault is a major tectonic boundary, strike-slip movements along this fracture zone were limited between Early Jurassic and Oligocene times (Olivet, 1996). On the continent, the Messejana and Nazare faults are considered to be re-activated Hercynian structures connected to the AGFZ (Fig. 1–2).

Widespread occurrences of alkaline rocks are found in the eastern North Atlantic and in Portugal, corresponding to the Madeira Archipelago, the TMR seamounts and surroundings and the three massifs of Portugal studied here (Fig. 1). Different isotopic methods, such as U–Pb, K–Ar and ^{40}Ar–^{39}Ar on minerals and whole rocks have been used to determine the emplacement age of the oceanic rocks. Recently, Merle *et al.* (2009) produced a comprehensive geochronological review of the TMR seamounts and surroundings. The interpretation of some ages may be problematic due to the use of different isotopic systems, the unreliability of some dating methods, and the possible alteration of oceanic rocks. However, the ages reported in Fig. 1 are considered to be reliable estimates of magmatic events; we refer to Merle *et al.* (2009) for further discussion of these ages. The resulting age compilation generated for the TMR seamounts and surroundings shows that these oceanic alkaline rocks have been emplaced over an interval from the late Lower Cretaceous (~103 Ma) until present times. Merle *et al.* (2009) interpreted the emplacement of the alkaline magmatic rocks to be related to the motion of the Iberian plate above a mantle thermal anomaly. The northward motion of the Iberian plate would have been interrupted by the closure of the Neo-Tethys basin and the subsequent Pyrenean orogeny, and could explain the present-day distribution of the alkaline magmatic massifs and seamounts.

The Portugal alkaline massifs: previous petrological and geochemical data

The alkaline rocks occur in several massifs, several tens of square kilometres in extent, located along the Portugal coast from the Lisbon area to the Algarve province, 250 km to the south

(Fig. 2a). The main magmatic complexes are, from north to south, the Sintra, the Lisbon volcanic complex, the Sines, and the Monchique massifs. Isolated bodies also occur, such as the Ribamar intrusion (50 km north of Sintra), and the dikes in the Algarve region. The main massifs (Sintra, Sines and Monchique) comprise a large variety of rocks with compositions ranging from granite to SiO_2-undersaturated phonolite and nepheline syenite. Magnetic anomalies and susceptibilities show that the Sintra and Sines massifs extend far into the sea, which means that not all potentially present rock types could be sampled (Silva *et al.*, 2000). Several attempts have been made over the past few decades to date the alkaline magmatism on the western coast of Portugal and a detailed review of this earlier work is provided by Miranda *et al.* (2009). The ages reviewed in the study of Miranda *et al.* (2009) are K–Ar ages on whole rock or separated minerals and Rb–Sr ages on whole rocks. These methods have proven to be unreliable for rocks older than a couple of Ma (e.g., Baksi, 2007).

Some isolated intrusions occur north of Lisbon, including the Ribamar dioritic intrusion and the Paco d'Ilhas monzogabbroic-monzonitic sill (Miranda *et al.*, 2009). Miranda *et al.* (2009) proposed an age of 88.0 ± 2.7 Ma for the Paco d'Ilhas sill (K–Ar on biotite), whereas the Ribamar intrusion has not been investigated so far (Fig. 2a). Farther south, the Lisbon volcanic complex is composed of flows, plugs, sills and dikes comprising alkali basalt, gabbro, dolerite, trachyandesite, trachyte, and rhyolite (Palacios, 1985). A single attempt to date this magmatic activity has been made by whole-rock K–Ar method leading to an unreliable age (see details in Miranda *et al.*, 2009).

The Sintra subvolcanic complex is located along the shore west of Lisbon, and has a semi-circular structure (Fig. 2b). The core is composed of syenite surrounded by granite (e.g., Wright, 1969; Sparks & Wadge, 1975) and is intruded by mafic rocks. No reliable ages were available until the recent study of Miranda *et al.* (2009) which documents an age of 79.2 ± 0.8 Ma (95% confidence) from the granite, obtained by the U–Pb method on zircon using LA-ICP-MS. The Foz da Fonte intrusion is a tephritic sill localised between the Sintra massif and the

Sines massif. This intrusion has been recently dated by ^{40}Ar–^{39}Ar step-heating method on amphibole separates (Miranda *et al.*, 2009). The weighted mean plateau yield an age at 93.6 ± 4.6 Ma (2σ) and the inverse isochron gives an age of 93.8 ± 7.8 Ma.

The Sines complex occurs about 100 km to the south of Lisbon along the coast. It displays a ring-shaped pattern comprising syenite, diorite-gabbro, basalt, and heterogeneous mafic breccias (Fig. 2c; Canilho, 1972; Rock, 1978). The syenite intrudes the gabbro and both are commonly cut by breccia dikes with basaltic to syenitic fragments. Several attempts to date the Sines complex have been made over the past three decades using the K–Ar technique. The results are summarized in Miranda *et al.* (2009). An U–Pb age on zircon of 75.4 ± 0.6 Ma (95% confidence) obtained by LA-ICP-MS is the most reliable age constraining the emplacement of this massif (Miranda *et al.*, 2009).

The Monchique complex is the largest massif (63 x 16 km), with an E–W elliptical shape (Fig. 2d) and has been defined as a subvolcanic laccolith emplaced into Upper Carboniferous marine sediments (Rock, 1978). It is mainly composed of nepheline syenite, alkali gabbro, and diorite, but it also contains trachytic and syenitic breccias that host basalt, syenite, phonolite, and pelite fragments (Rock, 1978). This massif is intruded by phonolite plugs and lamprophyre dikes. Previous dating of the Monchique complex yielded K–Ar ages on minerals and whole-rock Rb–Sr isochron ages of ~ 72 Ma (Miranda *et al.*, 2009 and references therein). The nepheline syenite body was emplaced at 72.3 ± 8.4 Ma (2σ) based on a recent age obtained by whole-rock Rb–Sr isochron (Miranda *et al.*, 2009). The ultramafic components of the Monchique complex yield an age at 74.4 ± 4.0 Ma (2σ) showing that they were likely emplaced at the same time (^{40}Ar–^{39}Ar age on amphibole, Miranda *et al.*, 2009). At 72 Ma, whole-rock isotope analyses define initial $^{87}Sr/^{86}Sr$ (Sr_i) between 0.70312 and 0.70337, and initial epsilon Nd (εNd_i) range between +4.3 and +5.6 (Rock, 1976; Bernard-Griffiths *et al.*, 1997, Miranda *et al.*, 2009). Initial Pb isotope ratios (Pb_i) of whole-rock are 19.409–19.732

for $^{206}Pb/^{204}Pb$, 15.623–15.651 for $^{207}Pb/^{204}Pb$, and 39.38–39.80 for $^{208}Pb/^{204}Pb$ (Bernard-Griffiths *et al.*, 1997).

Sparse basaltic dikes, between one to a few meters in width, occur in the Algarve region but represent significantly smaller magmatic volumes compared to the three main massifs. Previous geochronological data available for these dikes were made using the K–Ar technique on whole-rock yielding ages between 77 ± 3 and 72 ± 2 Ma (no data published, cited in Martins, 1991). The age of these magmatic rocks was refined to 71.8 ± 3.8 Ma (2σ) by K–Ar on biotites extracted from a lamprophiric dike sampled in the Loulé area (Miranda *et al.*, 2009).

ANALYTICAL PROCEDURES

Major and trace element analyses were carried out using the SARM facilities (Service d'Analyses des Roches et Minéraux) at the CRPG (Centre de Recherches Pétrographiques et Géochimiques, Nancy, France), by inductively coupled plasma atomic emission spectrometry (ICP-AES) and inductively coupled plasma mass spectrometry (ICP-MS), following the procedures described in Govindaraju & Mevelle (1987) and in Carignan *et al.* (2001). Precision of major element analyses is 1–5% except for MnO, MgO, CaO, and P_2O_5 (10%). Trace element analyses have precision of 5–10% for >50 ppm abundance, 5–15% for 10–50 ppm, 5–20% for 1–10 ppm, and 5–25% for <1 ppm. Mineral separation was carried out using the Frantz isodynamic magnetic separator, heavy liquids ($CHBr_3$ and CH_2I_2), and grain-by-grain hand-picking under the binocular microscope. All chemical procedures for isotope analyses and mass spectrometric measurements were done at the University of Nice – Sophia Antipolis, except for the Hf measurements obtained on the MC-ICP-MS instruments at the Ecole Normale Supérieure (ENS-Lyon, France).

All grains used for isotope analyses (zircon, titanite, K-feldspar, and plagioclase) represent the most euhedral, transparent, and inclusion- and crack-free grains of the populations. To minimise the influence of surface alteration or weathering, individually selected grains were abraded (zircon and titanite) and leached. Prior to hand-picking selection, zircons were mechanically abraded (Krogh, 1982), washed at 100°C for 1h in 7N HNO_3, rinsed in triple distilled water and weighed on a Cahn 50 microbalance. After transfer of the 1–30 zircon grains to the PTF® pressure capsules, the ^{205}Pb–^{233}U–^{235}U isotope tracer solution was added and dried on the hot-plate. Dissolution and homogenization with the spike solution was achieved with 25N HF during three days at 215°C. After drying the HF, 3N HCl was added, and the capsules were closed and heated at 215°C for one day to dissolve the fluorides. This solution was then directly introduced on the AGW-1X8 200–400 mesh anion resin and chemical treatment was performed as described by Krogh (1973). This chemical procedure also separates U and Pb from Zr and Hf. Hafnium contained in the 3N HCl fraction was further processed through AGW-50X-12 cation resin® to eliminate ^{176}Yb interferences on ^{176}Hf (Patchett & Tatsumoto, 1980). Because Lu/Hf is very low in zircon (e.g., Patchett *et al.*, 1981; Schärer *et al.*, 1997), the present-day $^{176}Hf/^{177}Hf$ values directly reflect those of the magma sources at the time of melting. For details on U–Pb–Hf systematics on zircons and associated chemical procedures, we refer to Bodet & Schärer (2000).

For titanite, the abrasion, washing, weighing, and isotope tracer addition are identical to those for zircon but the 2–20 grain titanite fractions were dissolved at 140°C for 15h with 25N HF in 2ml Savilex® beakers, followed by drying the HF, and then addition of 6N HCl to dissolve the fluorides for 4h at the same temperature as dissolution. The following chemical procedure used the same anion resin as for zircon but an HBr chemical procedure and an additional purification step for U (Manhès *et al.,* 1978). This latter chemical procedure was also used for K-feldspar and plagioclase, which were washed with 6N HCl and water, ground in an agate mortar and leached with a 1% HBr solution for 1–2 minutes (Schärer, 1991). After

decanting the wash solution, additional washing was performed with triple distilled water and the ^{205}Pb–^{233}U–^{235}U tracer solution was added. After drying, about 1.5 ml of 25N HF was added in 2ml Savilex® beakers and kept on the hot plate for 15h at 140°C. Note that one-third of the 3N HCl solution volume from the U–Pb chemistry was spiked with a ^{85}Rb–^{84}Sr tracer solution so that U–Pb and Rb–Sr isotope signatures could be measured on the same mineral fractions. For Rb–Sr concentration analyses on the spiked solution, Rb and Sr were separated using the Eichrom Sr-Spec resin®. Isotopic composition measurements were performed on the remaining unspiked two-thirds of the original solution volume and Rb was separated from Sr using the Eichrom resin. Plagioclase and K-feldspar fractions extracted from the U–Pb dated samples and from an additional undated phonolite from the Monchique complex (PT-22B) were analysed for U–Pb and Rb–Sr (Tables 4 and 5). Initial Pb_i and Sr_i ratios have been obtained by correcting the measured ratios for the *in situ* decay of U and Rb, measured on the same fraction, to the time of formation defined by the U–Pb age of the rock.

Zircon fractions vary in weight between 0.061 and 0.101 mg and titanite between 0.170 and 0.360 mg, representing between 1 and 30 grains per fraction for zircon and 2 to 20 grains for titanite. Grain sizes of zircon are between 0.05 and 0.20 mm and titanite between 0.10 and 1.5 mm. Both minerals are essentially euhedral and transparent crystals, with zircon varying between colorless and slightly yellow. Pleochroic titanite crystals range from yellow to brown in color. Opaque and transparent inclusions reach up to about 5 vol.% and were excluded from analyses as much as possible.

Overall analytical uncertainties of zircon U–Pb dates are 1–3.5% for $^{206}Pb/^{238}U$, 2–9 % for $^{207}Pb/^{235}U$, and have correlation coefficients between 0.3 and 0.7. For titanite, the corresponding errors and correlation coefficients are 2.5–3.5 %, 4–20 %, and 0.3–0.4, respectively. These uncertainties include in-run precisions, corrections for blanks and mass fractionation, and initial common Pb measured in the feldspar fractions. Lead blanks are 7–20 pg for zircon analyses and 30–60 pg for titanite. Concordia diagrams were plotted using Isoplot

Excel add-in (Ludwig, 2003); error ellipses on Figs. 5–7 take into consideration the above uncertainties and are plotted at the 2σ level. The age assigned to each sample corresponds to the weighted mean $^{206}Pb/^{238}U$ age of the different fractions, calculated with Isoplot and are reported at 95% level confidence, unless specified.

All U–Pb and Pb isotope analyses were carried out on single degassed (2000°C) Re filaments (H_3PO_4/Si-gel load) using a single secondary electron multiplier on a Thomson 206 mass spectrometer. Mass fractionation of 0.10 ± 0.05 % per amu was monitored by repeated analysis of the NBS-981 standard, which yielded average ratios of 16.941 ± 0.044 (2σ) for $^{206}Pb/^{204}Pb$, 15.501 ± 0.044 for $^{207}Pb/^{204}Pb$, and 36.728 ± 0.078 for $^{208}Pb/^{204}Pb$. Strontium isotope compositions were measured on a VG-Sector instrument using single Re filaments with a H_3PO_4/TaF_5 load. The NBS-987 standard was regularly analysed to monitor the accuracy of the Sr measurement and yielded an average $(^{87}Sr/^{86}Sr)_{norm}$ of 0.710289 ± 0.000082 (2σ). All Sr isotope measurements were normalised to $^{86}Sr/^{88}Sr = 0.1194$. Hafnium isotope measurements were performed on the Plasma VG-54 and the Nu plasma instruments at the ENS-Lyon using the JMC-475 Hf standard for calibration, run every fourth sample (Blichert-Toft *et al.,* 1997). This standard yielded a mean ratio of 0.282162 ± 0.000001 (2σ). All hafnium isotope measurements were normalised to $^{179}Hf/^{177}Hf = 0.7325$ (Patchett & Tatsumoto, 1980). For further comments on combined U–Pb–Hf isotope analyses on zircon we refer to Bodet & Schärer (2000). Decay constants of ^{238}U and ^{235}U are those determined by Jaffey *et al.* (1971), the constant for ^{87}Rb was taken from Steiger & Jäger (1977) and the ^{176}Lu decay constant is from Söderlund *et al.* (2004). Errors on isotopic ratios reported throughout the text and in Tables 4 to 6 correspond to analytical uncertainties, i.e., 2 standard error (internal measurement statistics).

RESULTS

Petrology and major and trace element geochemistry

Petrological notes of the studied samples

Synthesis on petrological classification and mineralogical notes of the rocks studied here are presented in Table 1. Textural variability within a single outcrop is commonly observed. The rocks are generally well preserved with minimal alteration. However, some samples show some visible alteration of the plagioclase and/or K-feldspar. Altered minerals were not selected for analysis and the leaching procedures allow us to assess that the isotope analyses are not biased by any form of alteration and therefore represent the primary isotopic composition of the magmas.

Major and trace element geochemistry

The rocks show a wide range of compositions as illustrated in the Na_2O+K_2O vs. SiO_2 diagram (TAS diagram, Fig. 3, Table 2). The Sintra samples lie in the basalt to rhyolite field, the Sines samples in the basalt to trachyte field, and the Monchique samples in the basanite to phonolite field. The Ribamar intrusion has basaltic to trachy-andesitic composition. With the exception of the granite from the Sintra massif, all rocks have an alkaline character, becoming more alkaline and SiO_2-undersaturated from north to south, i.e., from Sintra to Monchique. Among all the studied rocks, the alkali gabbro from Monchique (PT-21A) has the most primitive and SiO_2-undersaturated composition with MgO and CaO contents as high as 8.5 and 13.9 wt.% respectively, for only ~ 41 wt.% SiO_2. The most mafic rocks are evolved since they have MgO contents ranging from 4 to 8.5 wt.%. Their evolved compositions are confirmed by their compatible element contents (Ni = 6–75 ppm, Co = 22–50 ppm, Cr = 5–190 ppm) that are

lower than the range expected for magmas in equilibrium with their mantle source (Ni = 200–500 ppm, Co = 50–70 ppm, Cr = 500–800 ppm, e.g., Allègre *et al.*, 1977).

Chondrite-normalized rare earth element (REE) patterns and incompatible trace element concentrations relative to primitive mantle are shown on Fig. 4 for each studied massif, presented from Ribamar to the north to Monchique to the south. A common feature for the entire set of analysed rocks is their positive Pb anomaly. The Monchique alkali gabbro (PT-21A) is an exception with a slightly negative Pb anomaly, and represents the least differentiated and most mafic rock of this study. The Ribamar alkali diorite (PT-2A) shows a moderately steep REE pattern with $(La/Yb)_N$ = 16, and flat heavy REE (HREE) pattern. The trace element pattern is quite regular, showing no large anomalies (Fig. 4a–b).

Rocks from the Sintra massif have similar-shaped REE and incompatible element patterns (Fig. 4c–d). They are between 80 and 200 times enriched in light REE (LREE) compared to chondrite, with $(La/Yb)_N$ ranging from 5 to 19. The gabbro (PT-6A) does not have an Eu anomaly but has a slightly convex pattern for the middle REE (MREE). The three other rock samples have concave patterns and increasing negative Eu anomalies with (Eu/Eu*) at 0.62 for the syenite (PT-7A), 0.28 for the alkali granite (PT-9A), and 0.12 for the micro-granite (PT-5A). Except for the gabbro (PT-6A), the incompatible trace element patterns of the Sintra rocks show negative anomalies in Ba, Sr, P, and Ti (increasing in the same way as the Eu anomaly), and similar positive anomalies in Pb. Both the syenite (PT-7A) and the alkali granite (PT-9A) have parallel incompatible trace element patterns; the syenite being the most enriched sample in incompatible elements. Although the micro-granite appears to be the most differentiated rock type of the massif with more than 77 wt.% SiO_2 and only 0.06 wt.% MgO (Table 2), it is also the least enriched rock in REE contents compared to the three other samples, while the most primitive rock (alkali gabbro PT-6A) is the most enriched in REE. In fact, the more differentiated compositions, as indicated by MgO contents, correspond to less

enrichment in REE and more negative Eu, Ba, Sr, and P anomalies. Moreover, the micro-granite (PT-5A) shows a flat pattern for the HREE with $(Dy/Yb)_N = 0.90$.

The three rocks of the Sines complex are 200 to 400 times enriched in REE compared to chondrites, with $(La/Yb)_N$ between 9 to 19 (Fig. 4e–f). The two alkali gabbros (PT-16A and PT-17A) show parallel incompatible trace element patterns, although the alkali gabbro PT-17A has a more enriched REE pattern that is slightly convex for the MREE with a slight negative Eu anomaly (Eu/Eu* = 0.86) compared to PT-16A. The syenite (PT-19A) is more enriched in LREE than the alkali gabbros, and has a pronounced concave shape for the MREE. This slight REE enrichment of the syenite compared to the alkali gabbros is also visible on the overall incompatible element pattern (Fig. 4). These three samples show negative anomalies in Ba, P, and Ti and positive Pb anomalies, all being most pronounced for the syenite.

The REE patterns of Monchique rocks are similar to those in previous studies (Bernard-Griffiths *et al.*, 1997, Fig. 4) showing up to 400 times LREE enrichment compared to chondrites, yielding $(La/Yb)_N$ between 19 and 34 (Fig. 4g–h). The nepheline syenite (PT-20A) has a concave U-shaped pattern, similar to patterns reported for other samples from the same massif (Rock, 1976; Cornen, 1982; Bernard-Griffiths *et al.*, 1997). This feature is also present on the phonolite (PT-22B). In contrast, the alkali gabbro (PT-21A) has a convex REE pattern. The nepheline syenite and phonolite have quite similar incompatible element patterns with negative anomalies in Ba and P, and to a lesser extent in Ti, and positive anomalies in Pb, all being more pronounced for the nepheline syenite. In contrast, the alkali gabbro has positive anomalies in Ba, Nb, and Ti and a negative anomaly in Pb.

U–Pb dating

Table 3 lists zircon and titanite U–Pb analytical results and Figs. 5–7 show the corresponding concordia plots. All zircon and titanite ages were derived from $^{206}Pb/^{238}U$ because $^{207}Pb/^{235}U$

commonly has excessive scatter, especially for titanite data. This scatter is a consequence of low U contents in titanite and therefore low radiogenic Pb contents. Consequently, the $^{207}Pb/^{235}U$ ages are more sensitive to common Pb correction than $^{206}Pb/^{238}U$, and less precise. Specific features of the concordia diagrams for some samples are discussed later.

Six zircon fractions from the Ribamar diorite (PT-2A, Fig. 5a) yield identically concordant ages defining a weighted mean $^{206}Pb/^{238}U$ age of 88.3 ± 0.5 Ma (95% conf., MSWD = 0.90). These six zircon grains were not abraded because of their very fine acicular shape, which almost certainly would have been destroyed by abrasion. Nevertheless, the results are quite concordant and provide a very precise final age. The zircon ages obtained for the rocks of the Sintra massif are shown in Fig. 5b–e. Seven zircons from the micro-granite (PT-5A) give concordant ages with one grain having a slightly younger age than the bulk of the zircons. This grain (zircon #5) is unusually rich in U (> 4570 ppm) and is most probably affected by recent Pb loss. Excluding this grain provides a weighted mean $^{206}Pb/^{238}U$ age of 82.0 ± 0.7 Ma (MSWD = 1.18) (Fig. 5b). For the alkali gabbro (PT-6A), 10 zircon fractions yield concordant ages, showing about 10% scatter along the concordia curve. Using the six identically concordant fractions, an average $^{206}Pb/^{238}U$ age of 83.4 ± 0.7 Ma (95% conf., MSWD = 0.64) is defined (Fig. 5c). The four other zircons give younger ages between 74.9 and 81.3 Ma. For the micro-syenite (PT-7A), six zircon fractions give identically concordant ages and three fractions are discordant, one of them having a significantly older age at 142.1 ± 2.1 Ma (Fig. 5d). The weighted mean $^{206}Pb/^{238}U$ age of the six identically concordant ages is 80.1 ± 1.0 Ma (95% conf., MSWD = 2.0). Finally, eight zircon fractions from the granite (PT-9A) yield concordant ages and one fraction (#4) is about 5 m.y. younger (Fig. 5e). The weighted mean $^{206}Pb/^{238}U$ age of the eight identical fractions is 81.7 ± 0.4 Ma (95% conf., MSWD = 0.96).

Concordia diagrams of the U–Pb results for zircon and titanite from the Sines massif are shown on Fig. 6. For one gabbro (PT-16A), five zircon fractions yield identical $^{206}Pb/^{238}U$

ages (including one fraction that is about 10% discordant; Fig. 6a) whereas one grain gives a significantly older concordant age of 131.2 ± 1.7 Ma (Table 3). The weighted mean $^{206}Pb/^{238}U$ age for the five identical fractions is 77.2 ± 0.6 Ma (95% conf., MSWD = 0.19). Nine fractions from the second gabbro (PT-17A) yield identically concordant $^{206}Pb/^{238}U$ ages (Fig. 6b), defining a weighted mean of 77.2 ± 0.4 Ma (95% conf., MSWD = 0.50). Seven zircon and five titanite fractions from the syenite (PT-19A) are mostly concordant and give a combined weighted mean $^{206}Pb/^{238}U$ age of 75.4 ± 1.2 Ma (95% conf., MSWD = 4.2). The average $^{206}Pb/^{238}U$ age of the titanite is 74.0 ± 2.4 Ma (95% conf., MSWD = 3.9) and that of zircon is 76.1 ± 1.3 Ma (95% conf., MSWD=2.7), suggesting that the time of crystallisation for both minerals is the same within error (Fig. 6c). Nevertheless, we consider the age derived from zircon analyses to date the formation of the rock, as there is more consistency in the zircon data from this rock. The entire range of calculated ages is between 71.5 ± 2.3 Ma (titanite #6) and 77.8 ± 1.6 Ma (zircon #5).

For the nepheline syenite from the Monchique complex (PT-20A), the 12 titanite fractions have identical $^{206}Pb/^{238}U$ ages, whereas they show scatter in $^{207}Pb/^{235}U$, reaching up to 20% discordance (Fig. 7a–b). The weighted mean $^{206}Pb/^{238}U$ age is 68.8 ± 1.0 Ma (95% conf., MSWD = 2.7). The six titanite fractions from the alkali gabbro (PT-21A) are slightly discordant, plotting to the right of the concordia curve and giving a weighted mean $^{206}Pb/^{238}U$ age of 70.0 ± 2.9 Ma (95% conf., MSWD = 4.9).

Pb, Sr and Hf isotope data

Isotopic results of Pb and Sr are presented in Tables 4 and 5. Initial Pb ratios (Pb_i) of the rocks are 18.522–19.299 for $(^{206}Pb/^{204}Pb)_i$, 15.555–16.007 for $(^{207}Pb/^{204}Pb)_i$ and 38.480–39.330 for $(^{208}Pb/^{204}Pb)_i$. Initial $^{87}Sr/^{86}Sr$ (Sr_i) of the feldspars lie between 0.70274 and 0.70481. Initial Hf

isotope ratios of 18 different zircon fractions yield εHf_i ranging between +3.7 and +9.6 (Table 6). Correlation diagrams for all these initial isotope signatures are given in Figs. 8 and 9.

In the Sintra massif, the most primitive rock (the alkali gabbro PT-6A) exhibits the highest $(^{207}Pb/^{204}Pb)_i$ signature (Fig. 8a), whereas the most differentiated rocks have much lower ratios, with compositions similar to the MORB field for the syenite (PT-7A). This trend is less obvious for $(^{87}Sr/^{86}Sr)_i$ but still valid (Fig. 8b), with three samples having similar elevated ratios whereas the most differentiated rock (micro-granite PT-5A) has a $(^{87}Sr/^{86}Sr)_i$ in the field of the MORB. The same trend is observed in the rocks from the Sines and Monchique massifs: the most primitive rocks (PT-16A, -17A and -21A) have the highest $(^{87}Sr/^{86}Sr)_i$, while the most differentiated rocks have low ratios down to the MORB field, with the Monchique rocks plotting in the lowest part of the MORB field. However, the Sines rocks all have similar $(^{207}Pb/^{204}Pb)_i$ signatures.

In addition to the intra-massif isotopic evolution, the distribution of Pb_i and Sr_i isotopic data between massifs (inter-massifs) can also be described. From Sintra to Sines and then to Monchique, the rocks have gradually lower $(^{207}Pb/^{204}Pb)_i$ and $(^{87}Sr/^{86}Sr)_i$ and higher $(^{206}Pb/^{204}Pb)_i$. The Monchique rocks contain both the highest $(^{206}Pb/^{204}Pb)_i$ (PT-20A at ~19.30) and the lowest $(^{207}Pb/^{204}Pb)_i$ and $(^{87}Sr/^{86}Sr)_i$ values (respectively PT-21A at 15.55 and PT-22B at 0.70274). They plot into the North Atlantic MORB field and are very similar to previous data obtained from Monchique rocks (Bernard-Griffiths *et al.*, 1997) and from Tore seamounts (NW-Tore, Merle *et al.*, 2006). Following this general pattern of isotopic characteristics observed inter-massifs, Sines rocks have less radiogenic $(^{206}Pb/^{204}Pb)_i$ and more radiogenic $(^{207}Pb/^{204}Pb)_i$ and $(^{87}Sr/^{86}Sr)_i$ as compared to the Monchique rocks. They are quite similar to the North Atlantic MORB field in $(^{207}Pb/^{204}Pb)_i$ (Fig. 8). The isotopic compositions of the Ribamar sample (PT-2A) are between the Sines and Sintra signatures. Finally, the Sintra rocks have the highest $(^{207}Pb/^{204}Pb)_i$ (as high as 16.0) and $(^{87}Sr/^{86}Sr)_i$ and the lowest $(^{206}Pb/^{204}Pb)_i$. Figure 8 also shows the field of the Cabo Ortegal ultramafic rocks (Santos *et al.*, 2002),

recalculated at 80 Ma, which represents a proxy for the Iberian SCLM, and data from Jurassic alkaline rocks, emplaced during the Atlantic Ocean pre-rift period and interpreted to originate from the metasomatized SCLM (Grange *et al.*, 2008). The new data are similar in $(^{206}Pb/^{204}Pb)_i$ to the Cabo Ortegal field, but some rocks from the Sintra massif are substantially higher in $(^{207}Pb/^{204}Pb)_i$, similar to the trend defined by the Jurassic rocks (JRS, Fig. 8); whereas all the massifs contain some rocks lower in $(^{87}Sr/^{86}Sr)_i$ than the Cabo Ortegal field.

Hafnium isotopic data, correlated with ages and Pb_i are shown in Fig. 9, using the epsilon (ε) notation relative to chondritic uniform reservoir (CHUR) and calculated for the time of crystallisation of the rocks (εHf_i). Figure 9a also shows the evolution of the Depleted Mantle (DM) through time, which represents the evolution of the depleted asthenospheric mantle. The Hf data were acquired on the zircon fractions used for U–Pb geochronology, although the samples from Monchique massif did not contain any zircons and therefore no Hf data are available for these rocks. All the εHf_i are positive (Fig. 9), ranging between +3.7 and +9.6 and plot between the CHUR and the DM evolution lines. These data indicate that the source(s) is (are) more enriched than the asthenosphere. The εHf_i signatures increase progressively from the Ribamar intrusion to the Sines massif, i.e., from north to south. The variations in εHf_i vs $(^{206}Pb/^{204}Pb)_i$, $(^{207}Pb/^{204}Pb)_i$ and $(^{208}Pb/^{204}Pb)_i$ (Fig 9b–d) show that the studied samples have significantly lower εHf_i than the fields of the Atlantic MORB and the Tore Madeira Rise rocks. Our data plot in the field of worldwide-OIB and they show the same initial Hf signatures as the Mbuji-Mayi kimberlite samples (Weis & Demaiffe, 1985; Schärer *et al.* 1997). As there is very few data with combined Pb and Hf isotopic analyses for rocks representing the SCLM (such as xenoliths), this field is taken as a proxy for the composition of the SCLM. An important characteristic of these Hf data is the large variation within the same sample of up to 4 epsilon units for sample PT-9A. These variations are well above the individual analytical uncertainties and are therefore considered to be significant.

DISCUSSION

Geochronological data

U–Pb ages of the magmatic zircon and titanite can be considered to date crystallisation of these minerals in the magmas (e.g., Krogh, 1973; Zhang & Schärer, 1996). Our new ages significantly refine the intrusion ages along the western coast of Portugal; they are in the range of those ages obtained by Miranda *et al.* (2009) but are more precise. These 10 new ages clearly substantiate alkaline magma emplacement between 88.2 ± 0.5 and 68.9 ± 1.1 Ma, covering a period of about 20 m.y. in the Late Cretaceous, during Coniacian–Maastrichtian times (Gradstein *et al.*, 2004).

Some zircon fractions yield slightly different ages compared to the bulk zircon fractions used for the mean age calculation of the rock (e.g., PT-5A, PT-6A, PT-7A, PT-9A, PT-16A and PT-19A). The reason for these differences is not clear, however the presence of a small amount of inherited radiogenic Pb in zircon could account for older ages given by some zircons (PT-7A and PT-16A). Another explanation could be a slight difference between the initial Pb composition of the zircon (and titanite) and the feldspar. As the zircon (and titanite) ages have been corrected with the initial Pb measured in the feldspar, a difference could result in minor discordance. This interpretation is the most likely explanation for the $^{207}Pb/^{235}U$ discordance in titanite from sample PT-21A. Lastly, a recent loss of Pb from some of the grains could lead to a younger fraction of zircons (e.g., PT-5A, PT-6A and PT-9A).

Our new U–Pb ages of the alkaline massifs define a clear north–south age gradient (Fig. 10a), from the Ribamar intrusion at ~ 88 Ma to the Monchique complex emplaced around 69 Ma. The four massifs therefore constitute a distinct 200 km NNW–SSE alignment of alkaline rocks parallel to the Portugal coast.

Alkaline magmatism of similar age and chemical composition is also present in the oceanic domain, westward from this alignment (Fig. 1). On the Mount Ormonde massif (constituting the eastern part of the Gorringe Bank), some alkaline rocks intrude the SCLM peridotites and have been dated at 65–62 Ma (^{40}Ar–^{39}Ar on amphiboles from diorites, Féraud *et al.*, 1982; 1986; see discussion in Merle *et al.*, 2009). Widespread occurrences of alkaline magmatic rocks have also been documented along the TMR from ~ 103 Ma to the Pleistocene (Geldmacher *et al.*, 2006; Merle *et al.*, 2006; 2009). In particular, the trachytic magmatic rocks on the Tore seamounts, located about 500 km WNW of the Ribamar intrusion (Fig. 1), have been dated by the U–Pb method at 88.3 ± 3.8 Ma (Merle *et al.*, 2006), which is similar to our oldest age obtained from the Ribamar intrusion. Our new ages suggest that the period of magmatic activity on the western coast of Portugal overlaps with the northern part of the TMR. The combined geochronological data from the alkaline occurrences in the TMR, the Ormonde seamount and our new U–Pb ages from the alkaline massifs in western Portugal bracket the timing of an important alkaline magmatic activity in the eastern part of the North Atlantic Ocean over ~ 26 m.y., between 88 and 62 Ma.

Magma Differentiation

The analysed samples show large variation in chemistry with SiO_2 and MgO ranging from 40.9 to 77.2 wt.% and 0.06 to 8.5 wt.% respectively. The most evolved rocks (phonolites, trachytes and granites) are likely produced through a fractional crystallisation process as shown by the negative anomalies in the incompatible element patterns (Fig. 4). The negative anomalies in Ba, Sr, and Eu observed in the incompatible element patterns of these rocks can be explained by the fractionation of plagioclase, whereas the negative anomalies in P and Ti may be related to the fractionation of apatite and ilmenite, and titanite respectively. In the most mafic rocks (MgO > 4 wt%, PT-6A, PT-16A, PT-17A and PT-21A), the concentration of compatible trace

elements (Ni, Cr and Co) precludes that these rocks may be primitive magmas. Moreover, some of these rocks display bell-shaped MREE patterns that can be explained by amphibole and titanite accumulation (samples PT-6A, PT-17A, PT-21A). This feature has already been outlined by Rock (1976) and Cornen (1982) in the genesis of the Serra de Monchique rocks. The U-shaped MREE patterns observed in the most evolved samples (PT-5A, PT-19A, PT-20A and PT-22B) is likely explained by amphibole fractionation as already documented for the Serra de Monchique samples (Cornen, 1982).

All these observations suggest that the studied samples were derived from fractional crystallisation/accumulation processes. Considering relatively limited dataset for each massif and the absence of intermediate members of the fractional crystallisation series (i.e., granodiorites–trachyandesites), it is difficult to constrain the possible petrogenetic link between the mafic rocks and the most evolved samples through a fractional crystallisation process. Moreover, as the mafic samples show evidence for crystal accumulation, it is unlikely that they represent a parental liquid. This hypothesis precludes any modelling of fractional crystallisation processes using these samples to match the composition of the evolved rocks. Nevertheless, significant crystal fractionation would have to occur to produce the most evolved rocks. The characteristics of the REE patterns from the Sintra massif (i.e., the most evolved composition contains the lowest enrichment in REE, Fig. 4c) can be explained by significant crystal fractionation. This process was sufficiently important so that the incompatible REEs are incorporated into solid phases (such as zircon, which fractionates REE) before final solidification of melts, leading to the most evolved liquid (represented by the granite PT-5A) to be the least enriched in REE but very differentiated as indicated by its relative enrichment in the most incompatible elements such as U, Th and Rb. However, the rocks from the Sines massif may be linked through fractional crystallisation. The REE patterns of both alkali gabbros (PT-16A and PT-17A) are consistent with their petrologic types and major element compositions, i.e., PT-16A is the least evolved rock, with olivine relics and ~ 6.2 wt.% MgO,

whereas PT-17A is more differentiated, containing quartz and only 4.5 wt.% MgO. The parallel trace element patterns of these two samples may indicate that PT-17A is derived from PT-16A by fractional crystallisation.

Magma sources

Constraints from the most primitive rocks

To constrain the source(s) of the Portugal magmatic rocks, we focus on the most primitive rocks for each massif, namely PT-6A for Sintra, PT-16A and 17A for Sines, and PT-21A for Monchique. Within each massif, these rocks have the highest MgO and lowest SiO_2 contents (Table 2) and are also the oldest, i.e., the first to be emplaced (Table 3). These rocks have also undergone the least amount of crystal fractionation, as shown by their REE and other incompatible element patterns (Fig. 4c–d). These features suggest that these rocks have minimal interaction with any contaminant, such as the continental lithosphere (the SCLM and/or the crust) and therefore their isotopic characteristics are probably the closest to the source of the magmas. Consequently we will investigate these rocks first, from Sintra and Sines and then to Monchique.

The most primitive rocks from Sintra, and to a lesser extent from Sines, have the highest $(^{207}Pb/^{204}Pb)_i$ of their respective massif, moderate $(^{206}Pb/^{204}Pb)_i$ and moderate to low Sr_i (with a maximum at 0.70454 for PT-6A). Moreover, their initial Hf signatures are all positive and are consistent with a mantle source, slightly less depleted than (or a bit enriched compared to) the source of the MORB (i.e., the asthenosphere). The association of moderate to low Sr_i together with high $(^{207}Pb/^{204}Pb)_i$ is inconsistent with mantle-derived magmas contaminated by the upper continental crust, as this interaction would produce both high $(^{207}Pb/^{204}Pb)_i$ and high Sr_i. Moreover, significant contamination by the continental crust would be required to produce

such high ($^{207}Pb/^{204}Pb)_i$ leading to negative εHf_i. Our samples all display positive εHf_i up to +9.6. Indeed, the contamination by the continental crust would also lead to high initial ($^{87}Sr/^{86}Sr)_i$, especially for the rocks with the highest ($^{207}Pb/^{204}Pb)_i$ (16.007 ± 0.053 for PT-6A for only 0.70454 in Sr_i).

Alkaline rocks with high ($^{207}Pb/^{204}Pb)_i$ associated with relatively low ($^{206}Pb/^{204}Pb)_i$ and moderate to low Sr_i are observed in the rocks from the Ormonde-Ampere and TMR seamounts, as well as in the Jurassic alkaline magmatic rocks occurring on the continent contemporaneous with continental rifting (Bernard-Griffith *et al.*, 1997; Geldmacher & Hoernle, 2000; Merle *et al.*, 2006; Grange *et al.*, 2008). It is worth noting that an increase in the ($^{207}Pb/^{204}Pb)_i$ is observed from the Madeira Archipelago toward the continental alkaline massif of Monchique through the Ampere and Ormonde seamounts (Geldmacher & Hoernle, 2000). Merle *et al.* (2006) also analysed highly radiogenic ($^{207}Pb/^{204}Pb)_i$ from trachytes sampled on the Sponge Bob seamount (TMD4-3 at 15.714 ± 0.020 and TMD4-8 at 15.828 ± 0.040) associated with Sr_i as low as 0.70231. Lastly, the highest ($^{207}Pb/^{204}Pb)_i$ of the region was identified from Jurassic continental alkaline rocks (syn-rift magmatism) with a value of 15.925 ± 0.013 (Grange *et al.*, 2008; sample PT-35B, Soure). Considering that these isotopic characteristics cannot be explained by mantle-derived magmas contaminated by the continental crust for the reasons explained above, and because the continental crust is not present for the rocks emplaced in the oceanic domain (TMR, Ormonde), the authors interpret these isotopic signatures to be induced by the SCLM, which displays low Rb/Sr and high $^{207}Pb/^{204}Pb$ at moderate $^{206}Pb/^{204}Pb$. Geldmacher & Hoernle (2000) explained the increasing ($^{207}Pb/^{204}Pb)_i$ trend toward the continent as progressive contamination by the SCLM of magmas derived from an OIB-type source. Merle *et al.* (2006) invoked the interaction of magmas from an OIB-type source (deep mantle plume component) with material from the SCLM of the Iberian margin, since the SCLM peridotites from the Galicia Bank display Sr_i as low as 0.70210 (Chazot *et al.*, 2005). Grange *et al.* (2008) were unable to identify a major crustal component and deduced the high

($^{207}Pb/^{204}Pb)_i$ signature to have been produced by the partial melting of the SCLM. We note here that the positive Pb anomaly characterising the incompatible elements patterns of the most primitive rocks could be a feature induced by the contamination of the magmas by the continental crust. However, the isotopic data allow us to rule out any contamination from this constituent. Therefore, we suggest that the SCLM created this positive Pb anomaly, as suggested for the basaltic rocks erupted during the Central Atlantic Magmatic Province (CAMP) activity in the south Portugal (Marzoli *et al.*, 2006 and unpublished data). However, although the origin of this anomaly can be explained by the source itself, it is also possible that it is created by crystal fractionation process as the rocks considered here are not primitive and do not reflect the parental magma composition.

Therefore, a signature with high ($^{207}Pb/^{204}Pb)_i$, moderate ($^{206}Pb/^{204}Pb)_i$, low to moderate Sr_i and positive εHf_i in our rocks from Sintra and Sines can be explained by a large contribution of the SCLM in the source of these rocks.

The most primitive rock from Monchique (PT-21A) must have a different petrogenesis because it has the lowest ($^{207}Pb/^{204}Pb)_i$ but the highest Sr_i among the samples from the massif, close to the range of the MORBs (up to 0.70356) and to the Tore seamounts signatures (Merle *et al.*, 2006). In addition, all the rocks from the Monchique massif have ($^{206}Pb/^{204}Pb)_i$ higher than 19.1, plotting in the most enriched part of the MORB field. The mean value for the enriched Depleted MORB Mantle (i.e., enriched DMM) in ($^{206}Pb/^{204}Pb)_i$ is 18.977, for a ($^{207}Pb/^{204}Pb)_i$ of 15.568 and a ($^{87}Sr/^{86}Sr)_i$ of 0.70307 (Workman & Hart, 2005). The MORBs (Fig. 8) that display higher Pb_i signatures than those of the average enriched DMM may represent either an extremely enriched DMM or a mixture between a DMM-type source and an OIB-type component, such as the rocks in the North Atlantic region sampled in the vicinity of some hotspots (e.g., Dosso *et al.*, 1999). The primitive alkali gabbro PT-21A from Monchique has high ($^{206}Pb/^{204}Pb)_i$ with low ($^{207}Pb/^{204}Pb)_i$ and low Sr_i signatures, similar to those expected for the most enriched MORBs. This rock is also the only one displaying a negative Pb

anomaly. Following the same arguments as given for the Sintra and Sines rocks, this anomaly could reflect a lesser contribution from the SCLM in the magma source of the Monchique rock. However and as already stipulated for the Sintra and Sines rocks, this feature can reflect mineral fractionation processes and not the source characteristics. Regardless of this anomaly, and considering the low $(^{207}Pb/^{204}Pb)_i$, similar to the very low $(^{207}Pb/^{204}Pb)_i$ observed in the MORBs, for such a high $(^{206}Pb/^{204}Pb)_i$ (Fig. 8a), the component with a radiogenic $(^{207}Pb/^{204}Pb)_i$ identified in the Sintra and Sines massifs is not present in the isotopic signatures of the alkali gabbro from Monchique.

As a consequence, the Monchique rocks are more likely to be produced by a source displaying enriched DMM-like features. The characteristics of this source with $(^{206}Pb/^{204}Pb)_i >$ 19.1 and $Sr_i \sim 0.7031$ are very similar to the source for the Monchique and Ormonde massifs identified by Bernard-Griffiths *et al.* (1997) as a sub-lithospheric deep mantle source (OIB-type source). This source was also identified in the isotopic signatures of the NW-Tore seamount which plot in the field of the Madeira Archipelago rocks, derived from the Madeira plume (Merle *et al.*, 2006)

Several studies have shown that this region is affected by a deep thermal anomaly (e.g., Montelli *et al.*, 2004) that could sustain the alkaline volcanic activity in the oceanic domain for more than 100 Ma and is interpreted to be related to the Madeira hotspot (e.g., Geldmacher & Hoernle, 2000; Geldmacher *et al.*, 2006; Merle *et al.*, 2006, 2009). Therefore, the enriched DMM-like component that we identify in the Monchique rocks could be either a plume with an enriched DMM signature or the sub-lithospheric mantle (asthenosphere) enriched by a deep mantle plume. Both possibilities account for the relatively high $(^{206}Pb/^{204}Pb)_i$ observed in the rocks. However, in both cases, the involvement of a deep rooted heat source (deep mantle plume) is required to produce such widespread magmatism since 100 Ma.

Constraints from the evolved rocks

The study of the most primitive rocks from each massif shows that there are two components involved in the genesis of the Portugal rocks. The first component is the SCLM, which dominates the isotopic signatures of the samples from Sintra, i.e., earlier in time and in the northern extent of the magmatic alignment; it is responsible for the highest $(^{207}Pb/^{204}Pb)_i$ signatures. The second one is a sub-lithospheric component, having an enriched DMM isotopic signature, i.e., relatively high $(^{206}Pb/^{204}Pb)_i$ for low $(^{207}Pb/^{204}Pb)_i$. This latter component is clearly identified in the samples from Monchique, i.e., later in the emplacement of the Portugal rocks and in the southern extent of the magmatic alignment.

The implication of the SCLM in the source is further documented by the evolved rocks from the Sintra and Sines massifs. The Sintra and Sines massifs are the only locations where zircons having ages older than the mean emplacement age of the rock (PT-7A and PT-16A, Table 3) and showing maximum variations in Hf signatures of 4 and 2 epsilon units (PT-9A and PT-17A, respectively; Table 6) are found. However, these heterogeneities are not measured within the same rocks. An obvious explanation is because the oldest zircon fractions (zircon #7 for PT-7A and zircon #2 for PT-16A, Table 3) were not selected for Hf analyses (Table 6) and some U-Pb age measurements failed, resulting in fractions used for Hf tracing having no U-Pb ages. The only rock showing complete data is PT-17A (alkali gabbro from Sines), for which all the zircon fractions selected for Hf data were also successfully dated. This rock shows that the zircon fractions with εHf_i varying within a range of 2 units have the same U-Pb age within error. However, as zircon grains with visible inherited cores or xenocrysts have either been discarded during hand-picking or not observed and as most of the fraction showing outlier ages have not been analysed for Hf and *vice versa*, the mechanism producing these heterogeneities is difficult to decipher for the small scale. Nevertheless, we can assess that such heterogeneities within the zircon population from the same rock most likely reflect

the heterogeneity of the source as it cannot be produced by any crystallisation-fractionation processes.

Therefore, the zircon must have crystallised from magmas with heterogeneous Lu/Hf and U/Pb, producing in particular different $^{176}Hf/^{177}Hf$ that would be incorporated into the zircon grains. These heterogeneities in Hf and Pb are most likely explained by the SCLM component, resulting from pervasive infiltration of fluids (metasomatism) over time and modification of the mantle composition by re-enrichment in the most incompatible elements. These periods of metasomatism of the Iberian SCLM can be associated with orogeny–subduction cycles identified in the latest Archean (~ 2.3 Ga), Paleo–Neoproterozoic (~ 1.9 and 0.6 Ga) and Hercynian (0.4–0.3 Ga) times (e.g., Kuijper *et al.*, 1982; Peucat *et al.*, 1990; Santos *et al.*, 1996), and possibly by percolating magmas associated with the Atlantic pre- and syn-rift period (Charpentier *et al.*, 1998; Chazot *et al.*, 2005). These successive phases of metasomatism would enrich the SCLM in LIL and HFS elements as the enriched magmatic fluids percolated through the lithosphere. As a result, polyphase enrichment of the SCLM produced varying time-integrated Rb/Sr, Sm/Nd, Lu/Hf, U/Pb and Th/Pb values. Therefore, the inherited radiogenic Pb and heterogeneous εHf_i likely result from the contamination of the alkaline magmas generated in the sub-lithospheric mantle during their ascent through the SCLM. This interpretation is supported by the observation that the oldest zircon fraction from the Sintra syenite (PT-7A) yields an age of 142 Ma, which is the same age as the pre-rift alkaline magmatism that originated from the SCLM (Grange *et al.*, 2008).

The data also indicate that the proportion of the SCLM and the sub-lithospheric mantle components vary from the Sintra to the Monchique massifs, i.e., from north to south, and also vary through time. The rocks from Sintra have the highest $(^{207}Pb/^{204}Pb)_i$, inherited Pb, and εHf_i varying up to 4 units; features all attributed to the SCLM. The rocks from Sines have lower $(^{207}Pb/^{204}Pb)_i$, εHf_i variation of only 2 units and no obvious inherited Pb. Although no Hf data is available for the rocks from Monchique, they show the most minor SCLM component with

the lowest ($^{207}Pb/^{204}Pb)_i$ for the highest ($^{206}Pb/^{204}Pb)_i$ and no inherited Pb. Therefore, these features suggest that the contribution of the SCLM within the source decreases from north to south, and also through time. This variation is also accompanied by an increasing contribution of the sub-lithospheric source. Indeed the average signatures in ($^{206}Pb/^{204}Pb)_i$ and εHf_i increase from Sintra (18.832 and +6.1, respectively) to Sines (18.935 and +8.4, respectively) and then to Monchique (19.216). The Sr_i ratios also decrease from north to south to reach an average value of 0.70321 for the Monchique rocks, which is a value close to the value proposed by Bernard-Griffiths *et al.* (1997) for their deep sub-lithospheric mantle component (~ 0.7031).

GEODYNAMICAL IMPLICATIONS

Origin of the north–south age trend

The magmatic intrusions along the Portugal margin were emplaced during a period of about 20 m.y. along a N–S trend, with the oldest rocks dated at 88 Ma occurring to the north and the youngest rocks of 69 Ma emplaced in the south. Age trends have been described for several seamount chains (e.g., Hawaii–Emperor chain, Walvis ridge) and are related to fixed and deep rooted mantle plumes above which the lithospheric plate moves at a relatively faster speed, and tracks a record of the hotspot activity through time. In our case, if the observed age gradient is ascribed to plate motion, it would require that the Iberian Peninsula moved about 200 km toward the NNW between approximately 88 and 69 Ma. According to the geodynamic model proposed by Sibuet *et al.* (2004), the direction of the Iberian plate was toward the NE prior to 88 Ma, at which time the kinematics of the Iberian plate changed due to the closure of the oceanic domain between Iberia and Europe. This event resulted in a period of quiescence in the Iberian plate motion from 88 Ma until ~ 81–80 Ma. At this time, the subduction of the Iberian plate under Europe was initiated, resulting in NNW motion of the plate that continues today

(Sibuet *et al.,* 2004). Our age data are consistent with the plate kinematics between 88–80 Ma and 68–60 Ma, when the Iberian plate was directed toward the NNW. The plate motion model proposed by Sibuet *et al.* (2004) has already been shown to be in accordance with the overall repartition of the alkaline magmatism in the region, including the occurrences of alkaline magmatism on the continent. Indeed, the distribution of the magmatism has been interpreted to be a result of the interaction between a mantle plume emitting pulses of magma and the complex motion of the Iberian plate (Merle *et al.,* 2009). Our data agree with this geodynamical model and therefore confirm the preliminary data of Grange *et al.* (2007) used by Merle *et al.* (2009).

The emplacement of the alkaline complexes in Portugal along the NNW–SSE direction may have occurred along major lithospheric discontinuities, since the magmatic rocks on land and offshore are located close to these structures. These major faults, such as the Messejana and Nazare faults (Fig. 1), are Late Hercynian structures reactivated during the extensional rifting phases of the continent during the Jurassic and are connected to the AGFZ system (Fig. 1). The role of these faults has already been invoked to explain the emplacement of the alkaline Jurassic magmas (syn-rift magmatism) occurring in Portugal (Grange *et al.*, 2008) and Cretaceous alkaline rocks of the Gorringe Bank and of the Tore seamounts (Féraud *et al.*, 1986; Geldmacher *et al.*, 2006; Merle *et al.*, 2006).

Origin of the north–south isotopic evolution

A model to explain the spatial and temporal variations in the proportion of the SCLM and the sub-lithospheric mantle is schematically shown on Fig. 10a, which summarises the data from this study and shows the isotopic and age variation with latitude. Figure 10b provides a schematic mechanism of emplacement of the alkaline rocks which can be described as follow.

During the first stage (Ribamar and Sintra massif), slow ascent rates of the magmas derived from the sub-lithospheric mantle through the less permeable SCLM result in significant chemical interaction between those two components. Consequently, the magmas inherit Pb and Hf components from the SCLM, as evidenced by some zircon fractions from the Sintra massif. Through time, the magmas that originated from the sub-lithospheric mantle thermally "erode" the SCLM and have a more direct path toward the surface. This model implies that the magmas coming from the deep mantle have less residence time in the SCLM, and contain a weaker isotopic fingerprint of the SCLM component (i.e., Sines rocks). Therefore, the signatures of the rocks evolve toward compositions closer to the sub-lithospheric component (Monchique massif). These variations are induced by the northward motion of the Iberian plate, resulting in the southward migration of the alkaline magmatism: the pathways of the deep magmas toward the surface become better developed through time, reducing the contamination by the SCLM.

An alternative way to explain the observed chemistry is to invoke a progressive variation of the composition of the sub-lithospheric component instead of variable contamination by the SCLM. Regardless of the composition of the enriched DMM-like component (deep mantle plume or a mixture of the asthenosphere with an OIB-like mantle plume), this explanation would likely imply variable degrees of melting, magma production and therefore, variations in heat production within the plume for which we have no evidence. The contamination of a sub-lithospheric mantle source by various amount of SCLM is the most straightforward way in our opinion to explain the overall data, although we cannot exclude the possibility of coeval variation within the deep mantle source component.

SUMMARY & CONCLUSIONS

The alkaline massifs located along the Atlantic coast of Portugal originate from magmas that were (i) generated in a sub-lithospheric mantle source displaying an enriched DMM-like isotopic signature and (ii) contaminated on their way to the surface by the metasomatized SCLM. An unusual finding of this study is the correlation between ages, initial isotope signatures and spatial location of the studied intrusions, which likely reflects variations in the amount of contamination by the SCLM of the magmas from the sub-lithospheric component. This deep mantle source involved in the genesis of the alkaline continental rocks is most probably the same as required to produce the rocks from TMR and surrounding seamounts. Several geodynamical models have been proposed to explain the origin of this alkaline magmatism (e.g., Geldmacher *et al.*, 2000, 2001) but only the model proposed by Merle *et al.* (2009) takes into account the overall alkaline magmatism occurring on both oceanic and continental lithospheres and the complex motion of the Iberian plate. This model has been partly constrained by the preliminary results of the present study. Therefore the present work precisely brackets the onshore alkaline magmatism and confirms that the overall period of alkaline magmatism extends almost continuously from the Cretaceous to the present day, from the north of the TMR to the active Madeira archipelago. Our study shows that the alkaline magmatism of the westernmost part of the Portugal belongs to the same alkaline province as that described in the neighbouring oceanic domain, west of the continent and is a key location to reconstruct the geodynamic history of the North Atlantic Ocean.

ACKNOWLEDGEMENTS

The Ministry of Education and Research is acknowledged for the Ph.D. grant of M. Grange. We are grateful to A. Ribeiro and L. Pinheiro for field assistance and documents and M. Manetti and J.P. Goudour for technical help. Comments of K. Hoernle, two anonymous reviewers as well as the associate editor G. Wörner greatly helped to improve the successive versions of this manuscript and achieve the publication of this work; the time and effort they

spent on it have been much appreciated. The authors also want to thank F. Korhonen for improving the English of the last version of the manuscript.

REFERENCES

Allègre, C.J., Treuil, M., Minster, J.F., Minster, B. & Albarède, F. (1977). Systematic use of trace elements in igneous processes: part I Fractional crystallisation processes in volcanic suites. *Contributions to Mineralogy and Petrology* **60**, 57–75.

Allègre, C.J., Manhès, G. & Göpel, C. (1995). The age of the Earth. *Geochimica et Cosmochimica Acta* **59**, 1445–1456.

Baksi, A.K. (2007). A quantitative tool for detecting alteration in undisturbed rocks and minerals—I: Water, chemical weathering, and atmospheric argon. In: Foulger, G.R. & Jurdy, D.M. (eds) Plates, Plumes and Planetary Processes. Geological Society of America, Special Papers, 430, 285–303.

Bernard-Griffiths, J., Gruau, G., Cornen, G., Azambre, B. & Macé, J. (1997). Continental lithospheric contribution to alkaline magmatism: isotopic (Nd, Sr, Pb) and geochemical (REE) evidence from Serra de Monchique and Mount Ormonde complexes. *Journal of Petrology* **38**(1), 115–132.

Beslier, M.-O., Girardeau, J. & Boillot, G. (1990). Kinematics of peridotite emplacement during North Atlantic continental rifting, Galicia, northwestern Spain. *Tectonophysics* **184**, 321–343.

Blichert-Toft, J. & Albarède, F. (1997). The Lu-Hf isotope geochemistry of chondrites and the evolution of the mantle-crust system. *Earth and Planetary Science Letters* **148**, 243–258.

Blichert-Toft, J., Chauvel, C. & Albarède, F. (1997). Separation of Hf and Lu for high-precision isotope analysis of rock samples by magnetic sector-multiple collector ICP-MS. *Contribution to Mineralogy and Petrology* **127**, 248–260.

Bodet, F. & Schärer, U. (2000). Evolution of the SE-Asian continent from U-Pb and Hf isotopes in single grains of zircon and baddeleyite from large rivers. *Geochimica et Cosmochimica Acta*, **64**, 2067–2091.

Boillot, G., Girardeau, J. & Kornprobst, J. (1988). The rifting of the Galicia margin: crustal thinning and emplacement of mantle rocks on the sea floor. In: Boillot, G., Winterer, J. et al. (eds), *Proceeding ODP Scientific Results* **103**, 741–746.

Canilho, M.H. (1972). Estudo geológico-petrográfico do maciço eruptivo de Sines. *Boletim Museu Laboratorio Mineralogia-Geologia Faculdade de Ciencas, Universidade de Lisboa* **12**(2), 77–161.

Carignan, J., Hild, P., Mevelle, G., Morel, J. & Yeghicheyan, D. (2001). Routine analyses of trace element in geological samples using flow injection and low-pressure on-line liquid chromatography coupled to ICP-MS: a study of geochemical reference materials BR, DR-N, UB-N, AN-G and GH. *Geostandard Newsletters* **25**, 187–198.

Charpentier, S., Kornprobst, J., Chazot, G., Cornen, G. & Boillot, G. (1998). Interaction entre lithosphère et asthénosphère au cours de l'ouverture océanique: données isotopiques préliminaires sur la Marge passive de Galice (Atlantique Nord). *Comptes Rendus de l'Académie des Sciences de Paris* **326**, 757–762.

Chazot, G., Charpentier, S., Kornprobst, J., Vannucci, R. & Luais, B. (2005). Lithospheric mantle evolution during continental break-up: the West Iberia non-volcanic passive margin. *Journal of Petrology* **46**(12), 2527–2568.

Cornen, G. (1982). Petrology of the alkaline volcanism of Gorringe Bank (Southwest Portugal). *Marine Geology* **47**, 101–130.

Dosso, L., Bougault, H., Langmuir, C., Bollinger, C., Bonnier, O. & Etoubleau, J. (1999). The age and distribution of mantle heterogeneity along the Mid-Atlantic Ridge (31–41ºN). *Earth and Planetary Science Letters* **170**, 269–286.

Féraud, G., Gastaud, G., Auzende, J.-M., Olivet, J.-L. & Cornen, G. (1982). $^{40}Ar/^{39}Ar$ ages for the alkaline volcanism and basement of Gorringe Bank, North Atlantic Ocean. *Earth and Planetary Science Letters* **57**, 211–226.

Féraud, G., York, D., Mével, C., Cornen, G., Hall, C.M. & Auzende, J.-M. (1986). Additional $^{40}Ar/^{39}Ar$ dating of the basement and the alkaline volcanism of Gorringe Bank (Atlantic Ocean). *Earth and Planetary Science Letters* **79**, 255–269.

Geldmacher, J. & Hoernle, K. (2000). The 72 Ma geochemical evolution of the Madeira hotspot (eastern North Atlantic): recycling of Paleozoic (= 500 Ma) oceanic lithosphere. *Earth and Planetary Science Letters* **183**, 73–92.

Geldmacher, J., Van den Bogaard, P., Hoernle, K. & Schmincke, H.U. (2000). The $^{40}Ar/^{39}Ar$ age dating of the Madeira Archipelago and hotspot track (eastern North Atlantic). *Geochemistry, Geophysics and Geosystems* **1**, 1999GC000018.

Geldmacher, J., Hoernle, K., Van den Bogaard, P., Zankl, G. & Garbe-Schönberg, D. (2001). Earlier history of the Canary hotpot based on the temporal and geochemical evolution of the Selvagen archipelago and neighboring seamounts in the eastern North Atlantic. *Journal of Volcanology Geothermal Research*, **110**, 55–87.

Geldmacher, J., Hoernle, K., Klügel, A., Van den Bogaard, P., Wombacher, F. & Berning, B. (2006). Origin and geochemical evolution of the Madeira-Tore Rise (eastern North Atlantic). *Journal of Geophysical Research* **111**, B09206.

GEOROC database (Geochemistry of rocks of the oceans and continents), Max-Planck Institut für Chemie, http://georoc.mpch-mainz.gwdg.de/georoc/Start.asp

Girardeau, J. & Gil Ibarguchi, J.I. (1991). *Pyroxene-rich peridotites of the Cabo Ortegal Complex (northwestern Spain): evidence for large-scale upper mantle heterogeneity.* In: M.A. Menzies, C. Dupuy and A. Nicolas (eds) *Orogenic Lherzolites and Mantle Processes,* J. Petrol. Spec. Vol., 135–154.

Girardeau, J., Cornen, G., Beslier, M.-O., Le Gall, B., Monnier, C., Agrinier, P., Dubuisson, G., Pinheiro, L., Ribeiro, A. & Whitechurch, H. (1998). Extensional tectonics in the Gorrinde Bank rocks, Eastern Atlantic ocean: evidence of an oceanic ultra-slow mantellic accreting centre. *Terra Nova* **10**, 330-336.

Gonçalves, F. (1967). Subsídios para o conhecimento geológico do maciço eruptivo de Monchique. *Comunicações dos Serviços Geologicos de Portugal, Lisboa*, T. LII, 169–184.

Govindaraju, K. & Mevelle, G. (1987). Fully automated dissolution and separation method for inductively coupled plasma atomic emission spectrometry rock analysis; Application to the determination of rare earth elements. *Journal of Analytical Atomic Spectrometry* **2**, 615–621.

Gradstein, F.M., Ogg, J.G. & Smith, A.G. (2004). *A geological time scale*. Cambridge University Press, Cambridge.

Grange, M., Schärer, U., Cornen, G., & Girardeau, J. (2007). Time–space migration of melting within the East Atlantic plume and magmatism of Portugal: U–Pb ages and Pb–Sr–Hf isotopes. *Geochimica et Cosmochimica Acta* **71**, Supplement 1, A351.

Grange, M., Schärer, U. Cornen, G. & Girardeau, J. (2008). First alkaline magmatism during Iberia–Newfoundland rifting. *Terra Nova* **20**, 494–503.

Holmes, A. (1946). An estimate of the age of the Earth. *Nature* **157**(3995), 680–684.

Jaffey, H., Flynn, K.F., Glendenin, L.E., Bentley, W.C. & Essling, A.M. (1971). Precision measurements of half-lives and specific activities of ^{235}U and ^{238}U. *Physical Reviews* **C4**, 1889–1906.

Krogh, T.E. (1973). A low contamination method for hydrothermal decomposition of zircon and extraction of U and Pb for isotopic ages determination. *Geochimica et Cosmochimica Acta* **37**, 485–494.

Krogh, T.E. (1982). Improved accuracy of U–Pb zircon ages by the creation of more concordant systems using air abrasion technique. *Geochimica et Cosmochimica Acta* **46**, 637–649.

Kuijper, R.P., Priem, H.N.A. & den Tex, E. (1982). Late Archean-Early Proterozoic source ages of zircons in rocks from the Paleozoic orogen of Western Galicia, NW Spain. *Precambrian Research* **19**, 1–29.

Lassiter, J.C., Blichert-Toft, J., Hauri, E.H. & Barsczus, H.G. (2003). Isotope and trace elements variations in lavas from Raivavae and Rapa, Cook Austral islands: constraints on the nature of the HIMU- and EM-mantle and the origin of mid-plate volcanism in French Polynesia. *Chemical Geology* **202**, 115–138.

Le Bas, M.J., Le Maitre, R.W., Streckeisen, A. & Zanettin, B. (1986). A chemical classification of volcanic rocks based on the total alkali-silica diagram. *Journal of Petrology* **27**, 745–750.

Ludwig, K.R. (2003). User's Manual for Isoplot 3.00. *Berkeley Geochronology Center Special Publication*, No 4, pp. 71.

Manhès, G., Minster, J.F. & Allègre, C.J. (1978). Comparative U-Th-Pb and Rb-Sr study of the Saint Séverin amphoterite: consequence for early solar system chronology. *Earth and Planetary Science Letters* **39**, 14–24.

Martins, L.T. (1991). *Actividade ígnea Mesozóic em Portugal (Contribuição petrológica e geoquímica)*. Ph.D. Thesis, University of Lisbon, pp. 418.

Marzoli, A., Rapaille, C., Reisberg, L. & Bertrand, H. (2006). Trace element and Sr-Nd-Pb-Os evidence for a lithospheric mantle source for the European CAMP basalts. *Geochimica et Cosmochimica Acta* **70**(18), Suppl. 1, A397.

Merle, R., Schärer, U., Girardeau, J. & Cornen, G. (2006). Cretaceous seamounts along the continent-ocean transition of the Iberian margin: U-Pb ages and Pb-Sr-Hf isotopes. *Geochimica et Cosmochimica Acta* **70**, 4950–4976.

Merle, R., Jourdan, F., Marzoli, A., Renne, P.R., Grange, M. & Girardeau, J. (2009). Evidence of multi-phase Cretaceous to Quaternary alkaline magmatism on Tore–Madeira Rise and

neighbouring seamounts from $^{40}Ar/^{39}Ar$ ages. *Journal of the Geological Society of London* **166**, 879-894.

Miranda, R., Valadares, V., Terrinha, P., Mata, J., do Rosario Azevedo, M., Gaspara, M., Kullberg, J.C. & Ribeiro, C. (2009). Age constraints on the Late Cretaceous alkaline magmatism on the West Iberian Margin. *Cretaceous Research* **30**, 575–586.

Miyashiro, A. (1978). Nature of alkaline volcanic rock series. *Contributions to Mineralogy and Petrology* **66**, 91–104.

Montelli, R., Nolet, G., Dahlen, F.A., Masters, G., Engdahl, E.R. & Hung, S.H. (2004). Finite-frequency tomography reveals a variety of plume in the mantle. *Nature* **303**, 338–343.

Olivet, J.L. (1996). La cinématique de la plaque ibérique – Kinematics of the Iberian plate. *Bulletin Centre Recherche et Exploration – Prod. Elf Aquitaine*, **20**(1), 131–195.

Palacios, T.P. (1985). Petrologia do Complexo Vulcanico de Lisboa. Faculdade de Ciencias da Universidade de Lisboa, Portugal, Tese de Doutoramento, 260p.

Patchett, P.J. & Tatsumoto, M. (1980). A routine high-precision method for Lu-Hf isotope geochemistry and chronology. *Contribution to Mineralogy and Petrology* **75**, 263–267.

Patchett, P.J., Kouvo, O., Edge, C.E. & Tatsumoto, M. (1981). Evolution of continental crust and mantle heterogeneity: Evidence from Hf isotopes. *Contributions to Mineralogy and Petrology* **78**, 279–297.

PetDB database (Petrological database of the Ocean Floor), http://www.petdb.org/

Peucat, J.J., Bernard-Griffiths, J., Gil Ibarguchi, J.I., Dallmeyer, R., Menot, D., Cornichet, P. & Iglesias Ponce de León, M. (1990). Geochemical and geochronological cross-section of the deep Variscan crust: the Cabo Ortegal high pressure nappe (Northwestern Spain). *Tectonophysics* **177**, 263–292.

Rock, N.M.S. (1976). The comparative strontium isotopic composition of alkaline rocks: new data from southern Portugal and east Africa. *Contributions to Mineralogy and Petrology* **56**, 205–228.

Rock, N.M.S. (1978). Petrology and petrogenesis of the Monchique alkaline complex, southern Portugal. *Journal of Petrology* **19**, 171–214.

Salters, V.J.M. & White, W.M. (1998). Hf isotopes constraints on mantle evolution. *Chemical Geology* **145**, 447–460.

Santos, J.F., Schärer, U., Gil Ibarguchi, J.I. & Girardeau, J. (1996). Evolution of the Cabo Ortegal ultramafic-mafic complex: U-Pb, Rb-Sr and Pb-Pb isotope data. *Chemical Geology* **129**, 281–306.

Santos, J.F., Schärer, U., Gil Ibarguchi, J.I. & Girardeau, J. (2002). Genesis of a pyroxenite-rich peridotite at Cabo Ortegal (NW Spain): Geochemical and Pb-Sr-Nd isotope data. *Journal of Petrology* **43**, 17–43.

Schärer, U. (1991). Rapid continental crust formation at 1.7 Ga from a reservoir with chondritic isotope signatures, eastern Labrador. *Earth and Planetary Science Letters* **102**, 110-133.

Schärer, U., Corfu, F. & Demaiffe, D. (1997). U-Pb and Lu-Hf isotopes in baddeleyite and zircon megacrysts from the Mbuji Mayi kimberlite: constraints on the subcontinental mantle. *Chemical Geology*, **143**, 1–16.

Schärer, U., Girardeau, J., Cornen, G. & Boillot, G. (2000). 138-121 Ma asthenospheric magmatism prior to continental break-up in the North Atlantic and geodynamic implications. *Earth and Planetary Science Letters* **181**, 555–572.

Sibuet, J.C., Srivastava, S. & Spakman, W. (2004). Pyrenean orogeny and plate kinematics. *Journal of Goephysical Reseach* **109**, B08104, doi:10.1029/2003JB002514.

Silva, E.A., Miranda, J.M., Luis, J.F. & Galdeano, A. (2000). Correlation between the Paleozoic structures from West Iberian and Grand Bank margins using inversion of magnetic anomalies. *Tectonophysics* **321**, 57–71.

Söderlund, U., Patchett, P.J., Vervoort, J.D. & Isachsen, C.E. (2004). The ^{176}Lu decay constant determined by Lu-Hf and U-Pb isotope systematics of Precambrian mafic intrusions. *Earth and Planetary Science Letters* **219**, 311–324.

Sparks, R.S.J. & Wadge, G. (1975). Geological and geochemical studies of the Sintra alkaline igneous complex, Portugal. Bulletin of Volcanology **39**(3), 385–406.

Steiger, R.H. & Jäger, E. (1977). Subcommission on geochronology convention on the use of decay constants in geo- and cosmochronology. Earth and Planetary Science Letters **36**, 359–362.

Sun, S.S. & McDonough, W.F. (1989). *Chemical and isotopic systematics of oceanic basalts: implication for mantle composition and processes*. In: Saunders, A.D., Norry, M.J. (eds.) *Magmatism in the ocean basins*. Geological Society Special Publications, London **42**, 313–345.

Tatsumoto, M., Knight, R.J. & Allègre, C.J. (1973). Time differences in the formation of meteorites as determined from the ratio of 207-lead to 206-lead. *Science* **180**, 1279–1283.

Weis, D. & Demaiffe, D. (1985). A depleted mantle source for kimberlites from Zaire: Nd, Sr and Pb isotopic evidence. *Earth and Planetary Science Letters* **73**, 269–277.

Workman, R.K. & Hart S.R. (2005) Major and trace element composition of the depleted MORB mantle (DMM). *Earth and Planetary Science Letters* **231**, 53–72.

Wright, J.B. (1969). Re-interpretation of a mixed petrographic province – The Sintra intrusive complex (Portugal) and related rocks. *Geologische Rundschau* **58**, 538–564.

Zhang, L.-S. & Schärer, U. (1996). Inherited Pb components in magmatic titanite and their consequence for the interpretation of U-Pb ages. *Earth and Planetary Science Letters* **138**, 57–65.

Figure 1

Schematic bathymetric map of the eastern North Atlantic (from Merle *et al.*, 2009). Faults are represented using solid lines and inferred faults using dashed lines, AGFZ = Azores-Gibraltar-Fracture-Zone. Seamount locations are indicated with triangles and ages are the ones reported by Merle *et al.* (2009; and references therein): following their recommendations, the ages in bold represent ages obtained on minerals (U–Pb on titanite and zircon and ^{40}Ar–^{39}Ar on plagioclase, hornblende and biotite) and are considered to be the most reliable, whereas the other ages have to be considered with caution because they represent ^{40}Ar–^{39}Ar ages obtained on matrix. The ages from Porto Santos and Madeira Island (shown in italic) are undifferentiated ages obtained by ^{40}Ar–^{39}Ar on whole rock and on minerals (after Geldmacher *et al.*, 2000).

Figure 2

Geological sketch maps of the different alkaline complexes along the Portugal coast (modified after Gonçalves, 1967; Canilho, 1972) with (a) the full extent of the alkaline intrusions and in particular the Ribamar intrusion, (b) the Sintra complex, (c) the Sines complex and (d) the Monchique magmatic complex.

Figure 3

Total alkali vs. SiO_2 diagram (Le Bas *et al.*, 1986) for the Portugal samples. The separation line between alkaline and subalkaline series is from Miyashiro (1978).

Figure 4

REE and trace element patterns of the analyzed rocks, normalized to chondrite abundance for REE and primitive mantle for all trace elements (Sun & McDonough, 1989).

Figure 5

Concordia diagrams for U–Pb analytical results of zircons for (a) the Ribamar alkali diorite and for the Sintra massif, (b) the micro-granite, (c) the alkali gabbro, (d) the syenite and (e) the granite. Ellipses correspond to analytical uncertainties. Stippled ellipses correspond to analyses not taken into account for the age calculation (see text for further details).

Figure 6

Concordia diagrams for U–Pb analytical results of zircons and titanites for (a, b) two alkali gabbros and (c) the syenite of the Sines massif. Ellipses correspond to analytical uncertainties. Grey ellipses correspond to analyses on titanites.

Figure 7

Concordia diagrams for U–Pb analytical results of titanites for (a) the nepheline syenite and (b) the alkali gabbro of the Monchique massif. Ellipses correspond to analytical uncertainties.

Figure 8

(a) Correlation diagram for initial Pb isotopic compositions measured in primary magmatic feldspars and (b, c) correlation diagrams for Pb_i and initial $^{87}Sr/^{86}Sr$ measured from the same feldspars. These initial ratios are corrected for *in situ* decay of U and Rb, respectively (Table 3). Symbols are larger than analytical uncertainties. For comparison the following fields are shown: (i) initial isotopic compositions of Atlantic N-MORB (GEOROC and PetDB databases), (ii) previous data obtained on Monchique rocks (Bernard-Griffiths *et al.*, 1997), (iii) N-Tore and NW-Tore seamounts (Merle *et al.*, 2006), (iv) values for subcontinental lithospheric mantle (SCLM) at Cabo Ortegal (Santos *et al.*, 2002) re-calculated at 80 Ma using the decay constants from Steiger & Jäger (1977). The data for the Jurassic rocks that originated from the SCLM of the Portugal are also shown (three data linked by the dotted line, Grange *et*

al., 2008). The geochron is the model of Holmes (1946) using a 4.56 Ga age for the Earth and primordial Pb measured in the Canyon Diablo troilite (Tatsumoto *et al.*, 1973)

Figure 9

Initial Hf isotopic compositions (εHf_i) measured in zircons. (a) εHf_i is plotted in relation to the evolution of a chondritic reservoir (CHUR) and the continuously LILE-HFSE depleted mantle (DM). (b-d) correlation diagrams between εHf_i and Pb initial isotopic compositions measured in feldspars. For comparison are shown the fields of initial compositions of (i) Atlantic MORB-sources (GEOROC database; Salters & White, 1998), (ii) worldwide OIB-sources (Salters & White, 1998; Lassiter *et al.*, 2003), (iii) the Mbuji Mayi kimberlite, representing the only combined Pb–Hf data available for the subcontinental mantle (Weis & Demaiffe, 1985; Schärer *et al.*, 1997), and (iv) the Tore-Madeira Rise, including the Cretaceous seamounts in its northern sector (Merle *et al.*, 2006) and younger seamounts of the southern part (Geldmacher *et al.*, 2006). The symbols are larger than analytical uncertainties.

Figure 10

(a) Synthesis of the data obtained for this study, showing the variations of the ages, the alkalinity and the isotopic signatures together with the latitude of the samples. The arrows point in the direction of increasing isotope ratios and alkalinity. (b) Sketch of a geodynamical model consistent with the observed results: the N–S geochemical variations are explained by the two-component source (enriched sub-lithospheric + SCLM), with the SCLM contamination of the deep mantle source becoming less significant through time, i.e. from N to S (see text for details). The arrows point toward increasing influence from enriched sub-lithospheric and SCLM components.

Table 1: Petrographic descriptions of the studied samples of Portugal (from N to S).

Sample	Locality	Texture	Primary phases[(a)]		Alteration phases	Minor phases and accessories	**Rock type**
RIBAMAR							
PT-2A	quarry	fine	plagioclase	→	white micas	oxides	**Alkali**
N 39°0.093'		grained	K-fsp.	→	sericite	calcite	**Diorite**
W 9°24.800'			clinopyroxene				
			biotite	→	chlorite		
SINTRA							
PT-5A	Biscaia	micro-	quartz			zircon	**Micro**
N 38°45.527'	village	granular	K-fsp.	→	sericite	oxides	**Granite**
W 9°28.402'		porphyric	plagioclase	→	white micas		
			sparse muscovite				
PT-6A	Biscaia	medium	plagioclase			apatite	**Alkali**
N 38°45.844'	quarry	grained	biotite			titanite	**Gabbro**
W 9°28.332'			clinopyroxene			zircon	
			amphibole	→	chlorite	epidote	
PT-7A	N-Cabo	fine	K-fsp.	→	sericite	zircon	**Syenite**
N 38°46.984'	da Roca	grained	biotite				
W 9°29.010'			amphibole	→	chlorite		
			quartz				
			sparse plagioclase				
PT-9A	main	medium	K-fsp	→	sericite	apatite	**Alkali**
N 38°45.200'	granite	grained	quartz			zircon	**Granite**
W 9°25.469'	intrusion		biotite	→	chlorite		
			plagioclase	→	white micas		
SINES							
PT-16A	quarry	coarse	plagioclase			apatite	**Alkali**
N 37°56.902'	S-Sines	grained	clinopyroxene			sparse titanite	**Gabbro**
W 8°51.179'			biotite	→	chlorite	oxides	
			sparse olivine				
PT-17A	hill	coarse	plagioclase	→	white micas	apatite	**Alkali**
N 37°57.086'	between	grained	amphibole			titanite	**Gabbro**
W 8°51.858'	harbor		biotite			zircon	
	and beach		clinopyroxene	→	amphibole	oxides	
			sparse quartz			calcite	
PT-19A	Pedras	fine	K-fsp	→	sericite	apatite	**Micro**
N 37°57.968'	Negras	grained	sparse plagioclase	→	white micas	titanite	**Syenite**
W 8°52.757'		and tiny	quartz			zircon	
		vesicles	amphibole			oxides	
			biotite	→	chlorite	calcite	
						epidote	
MONCHIQUE							
PT-20A	Navete	coarse	alk. fsp	→	sericite	titanite	**Nepheline**
N 37°18.602'	quarry	grained	nepheline			apatite	**Syenite**
W 8°34.169'			clinopyroxene			oxides	
			biotite	→	chlorite	zeolite	
						calcite	
PT-21A	east of	coarse	amphibole (poikilitic)			apatite	**Alkali**
N 37°18.904'	Foia hill	grained	plagioclase (poikilitic)			titanite	**Gabbro**
W 8°34.469'		porphyroïd	clinopyroxene			oxides	
			nepheline				
			biotite				
PT-22A	top of	microlitic	alk. fsp	→	sericite	apatite	**Phonolite**
N 37°19.395'	Foia hill	and	sparse plagioclase	→	white micas	calcite	
W 8°35.178'		porphyric	clinopyroxene (relics)				

[(a)] Most abundant primary phases are indicated at the top of the list.

Table 2: Major and trace element concentrations of the Portugal alkaline rocks.

Massif	Ribamar	Sintra				Sines			Monchique		
Sample (PT-)	2A	5A	6A	7A	9A	16A	17A	19A	20A	21A	22B
SiO_2 (wt%)	50·39	77·19	47·72	67·51	74·23	49·45	49·59	66·15	54·66	40·87	59·30
Al_2O_3	16·44	12·37	17·46	15·68	13·31	15·08	17·84	16·71	21·38	11·75	17·83
FeO_T	8·29	0·92	11·25	3·31	1·95	12·01	10·45	2·81	3·00	13·54	2·93
MnO	0·19	0·00	0·18	0·08	0·04	0·17	0·18	0·10	0·10	0·19	0·14
MgO	2·55	0·06	4·00	0·89	0·23	6·18	4·51	0·59	0·66	8·51	0·73
CaO	6·14	0·19	9·99	1·78	0·69	9·09	8·59	1·49	1·72	13·88	1·85
Na_2O	4·12	3·54	3·47	4·52	3·74	3·38	3·63	5·37	8·27	2·43	7·37
K_2O	2·99	4·65	1·28	4·77	4·75	1·65	1·68	5·18	6·61	1·59	5·79
TiO_2	1·98	0·07	2·83	0·63	0·23	3·00	2·53	0·58	0·73	4·62	0·84
P_2O_5	0·63	<DL	1·27	0·16	0·05	0·59	0·64	0·12	0·11	0·53	0·17
LOI	6·84	0·63	0·69	0·71	0·91	0·15	0·97	1·05	2·24	1·10	2·01
Total	100·50	99·60	100·14	100·02	100·14	100·76	100·61	100·15	99·48	99·00	98·95
Na_2O+K_2O	7·11	8·18	4·74	9·29	8·49	5·03	5·31	10·55	14·88	4·01	13·16
V (ppm)	93·3	0·85	222	34·2	9·46	233	183	24·4	41·7	359	38·59
Co	8·69	0·24	22·5	4·49	1·45	37·7	25·4	3·61	3·40	49·71	3·14
Cr	5·87	7·14	5·33	13·1	7·53	176	56·6	6·07	13·8	190·3	5·14
Cu	5·66	<DL	12·0	4·97	<DL	49·7	32·1	3·99	4·46	61·1	<DL
Ni	4·92	3·20	6·11	7·90	4·13	75·5	37·4	4·60	6·77	58·3	<DL
Cs	1·33	4·14	1·53	8·35	4·78	1·20	1·57	2·13	4·37	0·45	1·12
Rb	77·4	213	35·4	189	172	46·7	48·3	218	215	32·1	102
Sr	1039	12·7	951	214	63·7	618	744	306	642	1166	431
Ba	766	25·3	424	606	280	430	376	629	369	870	578
Th	9·39	21·7	4·77	20·9	21·1	5·60	6·54	31·5	28·1	4·33	11·4
U	2·42	4·36	1·52	6·83	6·63	1·67	1·91	6·72	8·76	1·01	3·53
Nb	79·5	50·2	57·9	70·4	38·7	52·4	68·8	112	125	74·9	105
Pb	7·75	27·4	6·93	29·8	30·8	5·34	6·19	16·5	24·3	2·68	10·4
Zr	380	113	452	402	191	249	246	510	557	273	357
Hf	8·76	4·95	10·1	9·51	6·19	6·02	6·69	12·3	8·3	7·40	7·52
Y	33·7	17·3	35·4	25·5	32·2	26·0	49·6	31·6	11·0	29·3	24·3
La	64·8	16·9	56·8	64·3	45·9	41·6	50·2	86·1	61·9	55·2	91·3
Ce	137	35·9	1 23	120	94·0	87·2	118	158	90·1	122	181
Pr	16·3	4·43	15·3	12·3	10·5	10·5	15·9	15·8	7·69	15·3	20·0
Nd	63·9	15·6	63·4	41·1	37·1	42·1	70·2	51·2	22·3	61·3	68·4
Sm	12·2	3·43	12·8	7·08	7·74	8·45	15·8	8·22	3·08	11·9	10·4
Eu	3·60	0·11	3·65	1·24	0·65	2·63	4·18	1·96	0·90	3·66	2·57
Gd	9·64	2·67	10·8	5·29	6·48	7·36	14·1	6·01	2·19	9·44	6·95
Tb	1·32	0·48	1·48	0·84	1·05	1·03	2·00	0·93	0·33	1·26	0·98
Dy	6·99	3·11	7·60	4·67	5·99	5·54	10·9	5·38	1·85	6·53	5·24
Ho	1·21	0·62	1·31	0·85	1·12	0·97	1·90	1·01	0·35	1·06	0·89
Er	3·19	1·92	3·33	2·44	3·21	2·47	4·79	2·98	1·08	2·62	2·31
Tm	0·44	0·32	0·43	0·37	0·48	0·33	0·63	0·46	0·17	0·34	0·31
Yb	2·87	2·30	2·74	2·48	3·26	2·11	3·86	3·30	1·29	2·05	1·96
Lu	0·42	0·34	0·40	0·38	0·48	0·31	0·55	0·51	0·19	0·29	0·29
$(La/Yb)_N$	16·22	5·27	14·88	18·63	10·09	14·19	9·32	18·69	34·38	19·35	33·47
Eu/Eu*	1·02	0·12	0·95	0·62	0·28	1·02	0·86	0·85	1·05	1·06	0·92

LOI: loss on ignition; <DL: under detection limit; major and trace element analyses were carried out at the CRPG at Nancy (Govindaraju & Mevelle, 1987; Carignan *et al.*, 2001). The N subscript indicates the ratio normalized to the chondrite values (Sun & McDonough, 1989).

$Eu/Eu^* = Eu_N / \sqrt{(Sm_N \times Gd_N)}$.

Table 3: U-Pb analytical results for zircon and titanite of the Portugal alkaline rocks.

Location / Sample [a] / Fraction	Weight (mg)	Content		Measured [c]	Radiogenic Pb in at.% [d]			Atomic Ratios [d]		Apparent Ages [d] (Ma)	
		U(ppm)	Pb[b](pg)	$^{206}Pb/^{204}Pb$	^{206}Pb	^{207}Pb	^{208}Pb	$^{206}Pb/^{238}U$	$^{207}Pb/^{235}U$	$^{206}Pb/^{238}U$	$^{207}Pb/^{235}U$
RIBAMAR											
PT-2A *(alkali diorite)*											
zircon 1[e]	0·0935	810·0	41	1640	46·0	2·2	51·8	0·01382	0·09065	88·5 ± 1·0	88·1 ± 1·9
zircon 2[e]	0·0229	666·2	48	289	45·1	2·1	52·7	0·01357	0·08727	86·9 ± 1·4	85·0 ± 2·9
zircon 3[e]	0·0336	588·2	65	285	44·5	2·2	53·3	0·01378	0·09143	88·2 ± 1·9	88·8 ± 3·6
zircon 4[e]	0·0252	631·8	27	537	48·3	2·3	46·3	0·01382	0·09172	88·5 ± 1·3	89·1 ± 2·7
zircon 5[e]	0·0120	882·0	10	936	38·8	1·9	59·3	0·01381	0·09199	88·4 ± 1·0	89·4 ± 1·3
zircon 6[e]	0·0370	731·8	16	1459	43·8	2·1	54·1	0·01382	0·09137	88·5 ± 0·9	88·8 ± 1·8
								Mean (95% conf.)		**88·3 ± 0·5 Ma**	
SINTRA											
PT-5A *(micro-granite)*											
zircon 1	0·0453	972·3	126	305	87·7	4·1	8·2	0·01298	0·08283	83·1 ± 2·0	80·8 ± 3·2
zircon 2	0·0427	1123	140	294	87·6	4·1	8·3	0·01277	0·08150	81·8 ± 2·2	79·6 ± 3·4
zircon 3	0·0153	1291	64	266	84·9	4·0	11·1	0·01271	0·08202	81·4 ± 2·2	80·0 ± 3·6
zircon 5[f]	0·0213	4576	56	259	83·9	4·0	12·1	0·01209	0·07827	77·5 ± 2·1	76·5 ± 3·5
zircon 6	0·0256	1803	82	474	86·7	4·1	9·2	0·01286	0·08427	82·4 ± 1·4	82·2 ± 2·3
zircon 7	0·0209	1636	50	569	87·9	4·2	7·9	0·01282	0·08380	82·1 ± 1·4	81·7 ± 2·2
zircon 8[f]	0·0061	893·8	57	93	86·3	4·1	9·6	0·01239	0·08049	79·4 ± 2·6	78·4 ± 6·5
								Mean (95% conf.)		**82·0 ± 0·7 Ma**	
PT-6A *(alkali diorite)*											
zircon 1	0·0622	299·7	100	182	72·3	3·5	24·2	0·01300	0·08609	83·3 ± 1·6	83·9 ± 3·4
zircon 2[f]	0·0311	401·8	87	132	79·2	3·6	17·2	0·01257	0·07766	80·5 ± 1·9	75·9 ± 4·5
zircon 3[f]	0·0201	453·1	58	136	77·3	3·8	18·9	0·01169	0·07931	74·9 ± 1·8	77·5 ± 4·5
zircon 4	0·0255	174·9	31	140	75·3	3·7	21·0	0·01327	0·08899	85·0 ± 2·0	86·6 ± 4·6
zircon 5[f]	0·0559	468·6	74	307	70·4	3·2	26·4	0·01270	0·07847	81·3 ± 1·8	76·7 ± 3·3
zircon 7	0·0711	368·0	27	805	72·4	3·5	24·1	0·01295	0·08665	83·0 ± 1·2	84·4 ± 1·7
zircon 8[f]	0·0848	438·8	161	198	75·1	3·4	21·4	0·01222	0·07695	78·3 ± 1·8	75·3 ± 3·4
zircon 9	0·0630	366·1	56	357	72·3	3·4	24·3	0·01303	0·08350	83·4 ± 2·1	81·4 ± 2·6
zircon 10	0·0644	444·3	59	417	70·4	3·3	26·3	0·01298	0·08352	83·1 ± 2·0	81·5 ± 2·5
zircon 11	0·0820	391·9	61	454	70·8	3·4	25·8	0·01298	0·08426	83·1 ± 1·9	82·1 ± 2·6
								Mean (95% conf.)		**83·4 ± 0·7 Ma**	
PT-7A *(micro-syenite)*											
zircon 1	0·0201	270·2	88	67	79·3	4·4	16·3	0·01231	0·09331	78·9 ± 2·4	90·6 ± 8·0
zircon 4	0·0287	132·8	19	176	82·1	3·9	14·0	0·01274	0·08313	81·6 ± 1·9	81·1 ± 5·0

Table 3, continued

Location / Sample [a] / Fraction	Weight (mg)	Content		Measured [c]	Radiogenic Pb in at.% [d]			Atomic Ratios [d]		Apparent Ages [d] (Ma)	
		U(ppm)	Pb[b](pg)	$^{206}Pb/^{204}Pb$	^{206}Pb	^{207}Pb	^{208}Pb	$^{206}Pb/^{238}U$	$^{207}Pb/^{235}U$	$^{206}Pb/^{238}U$	$^{207}Pb/^{235}U$
zircon 5	0·0256	340·7	29	261	95·4	4·4	0·2	0·01274	0·08034	81·6 ± 1·4	78·5 ± 3·2
zircon 6	0·0408	267·5	56	171	91·8	4·4	3·8	0·01244	0·08243	79·7 ± 1·3	80·4 ± 3·2
zircon 7[f]	0·0867	295·3	83	456	85·4	4·6	10·0	0·02229	0·16523	142·1 ± 2·0	155·3 ± 3·4
zircon 8	0·0347	323·0	16	578	89·0	4·3	6·7	0·01244	0·08256	79·7 ± 1·1	80·5 ± 1·7
zircon 9	0·0424	394·2	22	612	85·3	4·1	10·6	0·01241	0·08191	79·5 ± 1·2	79·9 ± 1·7
								Mean (95% conf.)		**80·1 ± 1·0 Ma**	
PT-9A *(granite)*											
zircon 1	0·0985	581·0	155	320	83·7	4·0	12·3	0·01286	0·08400	82·4 ± 1·3	81·9 ± 2·6
zircon 3	0·0941	708·7	66	827	85·7	4·1	10·2	0·01266	0·08288	81·1 ± 1·2	80·8 ± 2·1
zircon 4[f]	0·0802	443·7	54	528	85·2	4·2	10·6	0·01200	0·08102	76·9 ± 1·3	79·1 ± 2·1
zircon 5	0·0671	444·1	32	762	85·5	4·0	10·4	0·01268	0·08232	81·3 ± 1·2	80·3 ± 2·0
zircon 6	0·0883	505·9	228	174	83·8	3·9	12·3	0·01256	0·08051	80·4 ± 1·9	78·6 ± 3·2
zircon 7	0·0770	589·1	148	270	85·0	4·1	10·9	0·01290	0·08477	82·7 ± 1·5	82·6 ± 3·2
zircon 8	0·0504	768·6	97	342	86·0	4·1	9·9	0·01277	0·08336	81·8 ± 1·3	81·3 ± 2·3
zircon 9	0·0643	473·2	64	399	89·4	4·3	6·3	0·01274	0·08433	81·6 ± 1·2	82·2 ± 2·5
zircon 10	0·0642	774·5	33	1246	86·1	4·2	9·8	0·01280	0·08470	82·0 ± 0·9	82·6 ± 1·6
								Mean (95% conf.)		**81·7 ± 0·4 Ma**	
SINES											
PT-16A *(alkali gabbro)*											
zircon 2[f]	0·0255	205·5	22	313	76·6	3·7	19·7	0·02057	0·13646	131·2 ± 1·7	129·9 ± 2·6
zircon 3	0·0244	666·3	20	642	76·0	3·7	20·3	0·01207	0·08041	77·3 ± 1·4	78·5 ± 2·2
zircon 4	0·0285	673·2	53	301	78·3	4·2	17·5	0·01204	0·08895	77·1 ± 1·8	86·5 ± 3·5
zircon 7	0·0275	396·5	27	321	84·4	4·1	11·5	0·01201	0·07967	77·0 ± 1·5	77·8 ± 2·5
zircon 8	0·0369	640·7	32	576	81·0	3·9	15·1	0·01198	0·07914	76·8 ± 1·3	77·3 ± 2·3
zircon 9	0·0628	410·9	27	750	78·5	3·8	17·7	0·01210	0·07934	77·5 ± 1·1	77·5 ± 1·7
								Mean (95% conf.)		**77·2 ± 0·6 Ma**	
PT-17A *(alkali gabbro)*											
zircon 1	0·0930	278·6	258	95	80·9	4·0	15·2	0·01208	0·08118	77·4 ± 2·7	79·2 ± 6·9
zircon 2	0·0154	197·1	60	57	79·5	4·2	16·3	0·01207	0·08423	77·4 ± 3·2	82·1 ± 9·5
zircon 3	0·0831	240·7	37	430	83·0	4·0	13·0	0·01219	0·07962	78·1 ± 1·5	77·8 ± 2·3
zircon 4	0·0971	287·6	16	1359	78·7	3·8	17·5	0·01200	0·07849	76·9 ± 0·9	76·7 ± 1·6
zircon 5	0·0948	230·1	25	677	80·9	3·7	15·4	0·01211	0·07592	77·6 ± 1·7	74·3 ± 2·2
zircon 7	0·0818	282·4	20	883	81·4	3·8	14·8	0·01196	0·07598	76·7 ± 1·0	74·4 ± 1·7
zircon 8	0·1008	370·0	25	1156	77·4	3·7	18·9	0·01210	0·07934	77·5 ± 1·0	77·5 ± 1·6
zircon 9	0·0738	301·6	13	1305	81·2	3·9	14·9	0·01209	0·07950	77·4 ± 0·9	77·7 ± 1·6

Table 3, continued

Location Sample [a] Fraction	Weight (mg)	Content U(ppm)	Pb[b](pg)	Measured [c] $^{206}Pb/^{204}Pb$	Radiogenic Pb in at.% [d] ^{206}Pb	^{207}Pb	^{208}Pb	Atomic Ratios [d] $^{206}Pb/^{238}U$	$^{207}Pb/^{235}U$	Apparent Ages [d] (Ma) $^{206}Pb/^{238}U$	$^{207}Pb/^{235}U$
zircon 10	0·0847	333·3	13	1722	80·2	3·8	16·0	0·01202	0·07828	77·0 ± 0·8	76·5 ± 1·5
								Mean (95% conf.)		**77·2 ± 0·4 Ma**	
PT-19A *(micro-syenite)*											
titanite 1	0·2991	187·5	364	131	59·3	3·7	37·0	0·01153	0·09973	73·9 ± 1·8	96·5 ± 4·2
titanite 2	0·1728	222·6	383	94	63·1	2·9	34·0	0·01190	0·07495	76·3 ± 1·7	73·4 ± 4·7
titanite 4	0·2552	207·0	623	82	63·4	2·9	33·6	0·01162	0·07412	74·5 ± 2·1	72·6 ± 5·0
titanite 5	0·3555	197·1	1602	50	58·8	2·7	38·5	0·01122	0·07184	71·9 ± 2·3	70·4 ± 9·0
titanite 6	0·2922	215·9	940	67	61·0	2·8	36·2	0·01116	0·07071	71·5 ± 2·3	69·4 ± 8·8
								Titanite Mean (95 % conf.)		74·0 ± 2·4	
zircon 1	0·0966	117·7	479	37	85·7	4·4	9·9	0·01195	0·08455	76·6 ± 2·0	82·4 ± 16·0
zircon 2	0·0221	138·2	20	130	73·8	3·8	22·4	0·01184	0·08244	75·9 ± 2·0	80·6 ± 4·5
zircon 5	0·0245	199·4	23	178	73·9	4·2	21·8	0·01214	0·09429	77·8 ± 1·6	91·5 ± 3·9
zircon 7	0·0977	168·9	77	178	77·1	3·7	19·2	0·01182	0·07872	75·8 ± 1·8	76·9 ± 3·7
zircon 8	0·0894	130·8	133	83	79·8	4·1	16·1	0·01149	0·08087	73·6 ± 2·1	79·0 ± 6·6
zircon 9	0·0583	119·2	60	104	75·8	3·6	20·5	0·01156	0·07383	74·1 ± 1·8	72·3 ± 2·7
zircon 11	0·0850	114·8	13	591	84·7	4·1	11·2	0·01195	0·07932	76·6 ± 1·1	77·5 ± 1·6
								Zircon Mean (95 % conf.)		**76·1 ± 1·3**	
								Mean (95% conf.)		75·4 ± 1·2 Ma	
MONCHIQUE											
PT-20A *(nepheline syenite)*											
titanite 1	0·3496	30·22	546	33	35·0	2·4	62·6	0·01098	0·10352	70·4 ± 1·8	100·0 ± 19·6
titanite 2	0·2675	28·52	423	32	36·5	2·4	61·1	0·01066	0·09578	68·4 ± 2·1	92·9 ± 19·7
titanite 4	0·3327	30·27	582	31	35·0	2·3	62·7	0·01065	0·09495	68·3 ± 2·3	92·1 ± 19·0
titanite 7	0·2920	28·94	537	31	34·4	3·0	62·6	0·01136	0·13673	72·8 ± 2·0	130·1 ± 25·9
titanite 8	0·2632	27·73	545	30	37·7	1·8	60·5	0·01056	0·06871	67·7 ± 2·4	67·5 ± 14·4
titanite 9	0·3210	29·48	494	33	35·8	2·0	62·2	0·01060	0·08032	68·0 ± 1·7	78·4 ± 14·8
titanite 10	0·1937	28·43	292	31	37·1	1·4	61·6	0·01043	0·05286	66·9 ± 2·1	-
titanite 11	0·3298	29·08	564	31	33·3	2·0	64·7	0·01050	0·08674	67·3 ± 2·1	84·5 ± 17·9
titanite 13	0·2316	27·52	492	28	40·8	1·6	57·6	0·01061	0·05654	68·0 ± 2·2	-
titanite 14	0·3593	27·40	678	29	35·5	1·2	63·4	0·01086	0·04928	69·6 ± 2·1	-
titanite 17	0·2856	29·53	813	26	35·1	2·1	62·8	0·01058	0·08838	67·8 ± 1·9	86·0 ± 18·3
titanite 18	0·3240	27·20	470	32	36·8	1·9	61·2	0·01087	0·07884	69·7 ± 1·7	77·1 ± 14·3
								Mean (95% conf.)		**68·8 ± 1·0 Ma**	
PT-21A *(alkali gabbro)*											
titanite 1	0·3193	11·58	225	30	30·2	2·1	67·7	0·01047	0·09944	67·1 ± 2·8	96·3 ± 18·0

titanite 2	0·2995	16·66	188	37	32·4	1·8	65·8	0·01077	0·08293	69·0 ± 2·5	80·9 ± 15·1
titanite 3	0·2796	14·55	297	28	34·7	2·3	63·0	0·01034	0·09356	66·3 ± 2·5	90·8 ± 19·5
titanite 4	0·2650	13·97	105	44	35·7	1·9	62·4	0·01144	0·08133	73·3 ± 2·3	79·4 ± 10·0
titanite 5	0·2168	11·35	71	43	30·6	1·8	67·5	0·01121	0·09101	71·9 ± 2·5	88·4 ± 10·3
titanite 6	0·2453	12·65	89	43	35·4	2·1	62·6	0·01105	0·08821	70·8 ± 2·3	85·8 ± 10·4
								Mean (95% conf.)		**70·0 ± 2·9 Ma**	

[(a)] Analyses were performed on crack-free and euhedral zircons and titanites.
[(b)] Total amount of blank + initial Pb.
[(c)] Ratios corrected for mass-discrimination and isotope tracer contribution.
[(d)] Ratios corrected for mass-discrimination, isotope tracer contribution, blank, and initial common Pb determined in feldspars of the same rock (Table 4). Individual errors are given at 2σ level. The mean age is the weighted mean average of the entire set of fractions, excluding some indexed (f), given at 95% confidence level.
[(e)] Not abraded fractions.
[(f)] Fractions not used for age calculation (see text for further details).
For further details, we refer to “Analytical procedures”.

Table 4: Initial Pb isotope ratios of feldspars of the Portugal alkaline rocks.

Location Sample	Weight	Concentration [a]		μ [b]	Initial isotope ratios [c]			Source [d] signatures		
	(mg)	U	Pb (ppm)		$(^{206}Pb/^{204}Pb)_i$	$(^{207}Pb/^{204}Pb)_i$	$(^{208}Pb/^{204}Pb)_i$	μ	ω	κ
RIBAMAR										
PT-2A	10·5	0·068	6·47	0·675	18·861 ± 0·010	15·639 ± 0·007	38·920 ± 0·019	9·41	38·0	4·03
SINTRA										
PT-5A	9·88	0·156	22·8	0·436	18·522 ± 0·092	15·818 ± 0·045	38·669 ± 0·121	9·07	36·9	4·07
PT-6A	10·9	0·050	4·18	0·778	19·237 ± 0·087	16·007 ± 0·053	39·330 ± 0·125	9·78	39·6	4·05
PT-7A	16·7	0·968	7·93	7·858	18·906 ± 0·008	15·628 ± 0·005	38·629 ± 0·013	9·45	36·7	3·89
PT-9A	9·98	0·034	23·4	0·093	18·664 ± 0·008	15·668 ± 0·004	38·480 ± 0·008	9·21	36·2	3·93
SINES										
PT-16A	12·6	0·450	5·12	5·661	18·953 ± 0·018	15·628 ± 0·010	38·849 ± 0·019	9·49	37·6	3·96
PT-17A	10·7	0·023	2·83	0·510	18·801 ± 0·014	15·627 ± 0·013	38·653 ± 0·030	9·34	36·8	3·94
PT-19A	7·30	0·100	7·60	0·845	19·052 ± 0·008	15·623 ± 0·007	38·768 ± 0·015	9·58	37·3	3·89
MONCHIQUE										
PT-20A	10·9	0·018	7·37	0·155	19·299 ± 0·016	15·589 ± 0·014	39·153 ± 0·034	9·82	38·8	3·95
PT-21A	6·84	0·005	3·73	0·089	19·237 ± 0·014	15·555 ± 0·014	38·918 ± 0·025	9·76	37·8	3·88
PT-22B[(*)]	9·93	0·056	4·25	0·856	19·113 ± 0·014	15·660 ± 0·012	38·857 ± 0·027	9·64	37·6	3·90

[(*)] Not dated, age taken from PT-20A.

[a] Corrected for mass-discrimination, blank and isotope tracer contribution.

[b] $\mu = {}^{238}U/{}^{204}Pb$, used for correction of in-situ decay of U.

[c] Ratios corrected for mass discrimination, blank, isotope tracer contribution, and *in situ* decay of U using the U-Pb ages (Table 3); $(^{208}Pb/^{204}Pb)_i$ is corrected for *in situ* decay of ^{232}Th estimated from μ and from $^{208}Pb/^{206}Pb$ measured in feldspars.

[d] $\mu = (^{238}U/^{204}Pb)$, $\omega = (^{232}Th/^{204}Pb)$, $\kappa = (^{232}Th/^{238}U)$ were calculated using the single-stage evolution model of the Earth mantle (Holmes, 1946) with an age of 4·56 Ga (Allègre *et al.*, 1995). Primordial Pb isotopic compositions are taken from Tatsumoto *et al.* (1973).

For further details we refer to “Analytical procedures”.

Table 5: Rb-Sr analytical results of feldspars of the Portugal alkaline rocks.

Location Sample	Weight (mg)	Concentrations Sr	Rb(ppm)	$^{87}Rb/^{86}Sr$	Age (Ma) $^{206}Pb/^{238}U$	Isotope ratios [a] $(^{87}Sr/^{86}Sr)_{norm}$	$(^{87}Sr/^{86}Sr)_i$
RIBAMAR							
PT-2A	10·5	435	35	0·235	88·3	0·70433 ± 3	0·70404
SINTRA							
PT-5A	9·88	13·7	79	16·77	82·0	0·72286 ± 11	0·70329
PT-6A	10·9	724	2·4	0·010	83·4	0·70455 ± 4	0·70454
PT-7A	11·0	204	14	0·194	80·1	0·70479 ± 10	0·70457
PT-9A	10·0	42·6	77	5·275	81·7	0·71094 ± 7	0·70481
SINES							
PT-16A	12·6	595	12	0·060	77·2	0·70378 ± 3	0·70371
PT-17A	10·7	727	1·5	0·006	77·2	0·70392 ± 9	0·70391
PT-19A	7·30	348	28	0·236	76·1	0·70364 ± 7	0·70339
MONCHIQUE							
PT-20A	10·9	500	101	0·592	68·8	0·70391 ± 6	0·70333
PT-21A	6·84	1350	14	0·031	70·0	0·70359 ± 10	0·70356
PT-22B[*]	9·93	44·2	69	4·580	68·8	0·70722 ± 8	0·70274

[*] Not dated, age taken from PT-20A.

[a] Ratios corrected for isotope tracer contribution and for *in situ* decay of Rb using the U-Pb ages (Table 3).

For further details we refer to “Analytical procedures”.

Table 6: Initial Hf isotopic composition of zircons for the Portugal alkaline rocks.

Location Sample Fraction	$(^{176}Hf/^{177}Hf)_{norm}$ [(a)]	$(^{206}Pb/^{238}U)$ age (Ma)	εHf_i [(b)]
RIBAMAR			
PT-2A			
zircon 2	0·282837 ± 3	88·3	4·1 ± 0·1
zircon 3	0·282885 ± 10	88·3	5·8 ± 0·4
SINTRA			
PT-5A			
zircon 8	0·282859 ± 4	82·0	4·9 ± 0·1
zircon 9	0·282880 ± 3	82·0	5·6 ± 0·1
PT-6A			
zircon 1	0·282921 ± 7	83·4	7·1 ± 0·3
zircon 11	0·282940 ± 4	83·4	7·8 ± 0·1
PT-7A			
zircon 1	0·282910 ± 7	80·1	6·7 ± 0·2
zircon 2	0·282899 ± 10	80·1	6·3 ± 0·4
PT-9A			
zircon 1	0·282941 ± 4	81·7	7·8 ± 0·2
zircon 2	0·282823 ± 5	81·7	3·6 ± 0·2
zircon 10	0·282874 ± 3	81·7	5·4 ± 0·1
SINES			
PT-16A			
zircon 1	0·282922 ± 8	77·2	7·1 ± 0·3
zircon 9	0·282941 ± 5	77·2	7·8 ± 0·2
PT-17A			
zircon 1	0·282966 ± 5	77·2	8·7 ± 0·2
zircon 2	0·282918 ± 7	77·2	7·0 ± 0·2
zircon 10	0·282974 ± 5	77·2	9·0 ± 0·2
PT-19A			
zircon 1	0·282994 ± 9	76·1	9·7 ± 0·3
zircon 12	0·282982 ± 6	76·1	9·3 ± 0·2

[(a)] Uncertainties for $(^{176}Hf/^{177}Hf)_{norm}$ are given relative to the last digits.

[(b)] To calculate εHf_i from $(^{176}Hf/^{177}Hf)_{norm}$ the following constants were used: age of the Earth = 4.56 Ga; present-day $(^{176}Lu/^{177}Hf)^0_{CHUR}$ = 0.0332 ± 2; present-day $(^{176}Hf/^{177}Hf)^0_{CHUR}$ = 0.282772 ± 29; (Blichert-Toft & Albarède, 1997);
$(\varepsilon Hf)^T_{sample} = [(^{176}Hf/^{177}Hf)^T_{sample}/(^{176}Hf/^{177}Hf)^T_{CHUR} - 1]\times 10^4$, with $(^{176}Hf/^{177}Hf)^T_{CHUR} = (^{176}Hf/^{177}Hf)^0_{CHUR} - (^{176}Lu/^{177}Hf)^0_{CHUR} \times (e^{\lambda T} - 1)$ (Patchett *et al.*, 1981); $\lambda_{Lu} = 1.867 \times 10^{-11}\ y^{-1}$ (Söderlund *et al.*, 2004), with T being the U-Pb age of the zircon.
For further details we refer to “Analytical procedures”.

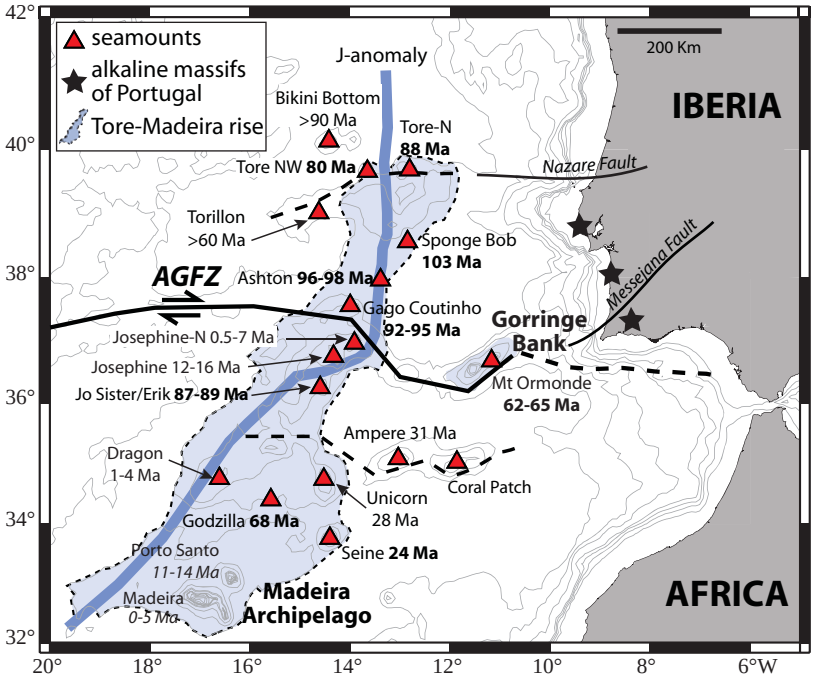
seamounts
alkaline massifs of Portugal
Tore-Madeira rise
J-anomaly
Bikini Bottom
>90 Ma
Tore-N
88 Ma
Tore NW 80 Ma
Nazare Fault
Torillon
>60 Ma
Sponge Bob
103 Ma
AGFZ
Ashton 96-98 Ma
Gago Coutinho
92-95 Ma
Messejana Fault
Gorringe
Bank
Josephine-N 0.5-7 Ma
Josephine 12-16 Ma
Jo Sister/Erik 87-89 Ma
Mt Ormonde
62-65 Ma
Ampere 31 Ma
Dragon
1-4 Ma
Coral Patch
Unicorn
28 Ma
Godzilla 68 Ma
Seine 24 Ma
Porto Santo
11-14 Ma
Madeira
0-5 Ma
Madeira
Archipelago
200 Km
IBERIA
AFRICA
42°
40°
38°
36°
34°
32°
20°
18°
16°
14°
12°
10°
8°
6°W

Figure 1

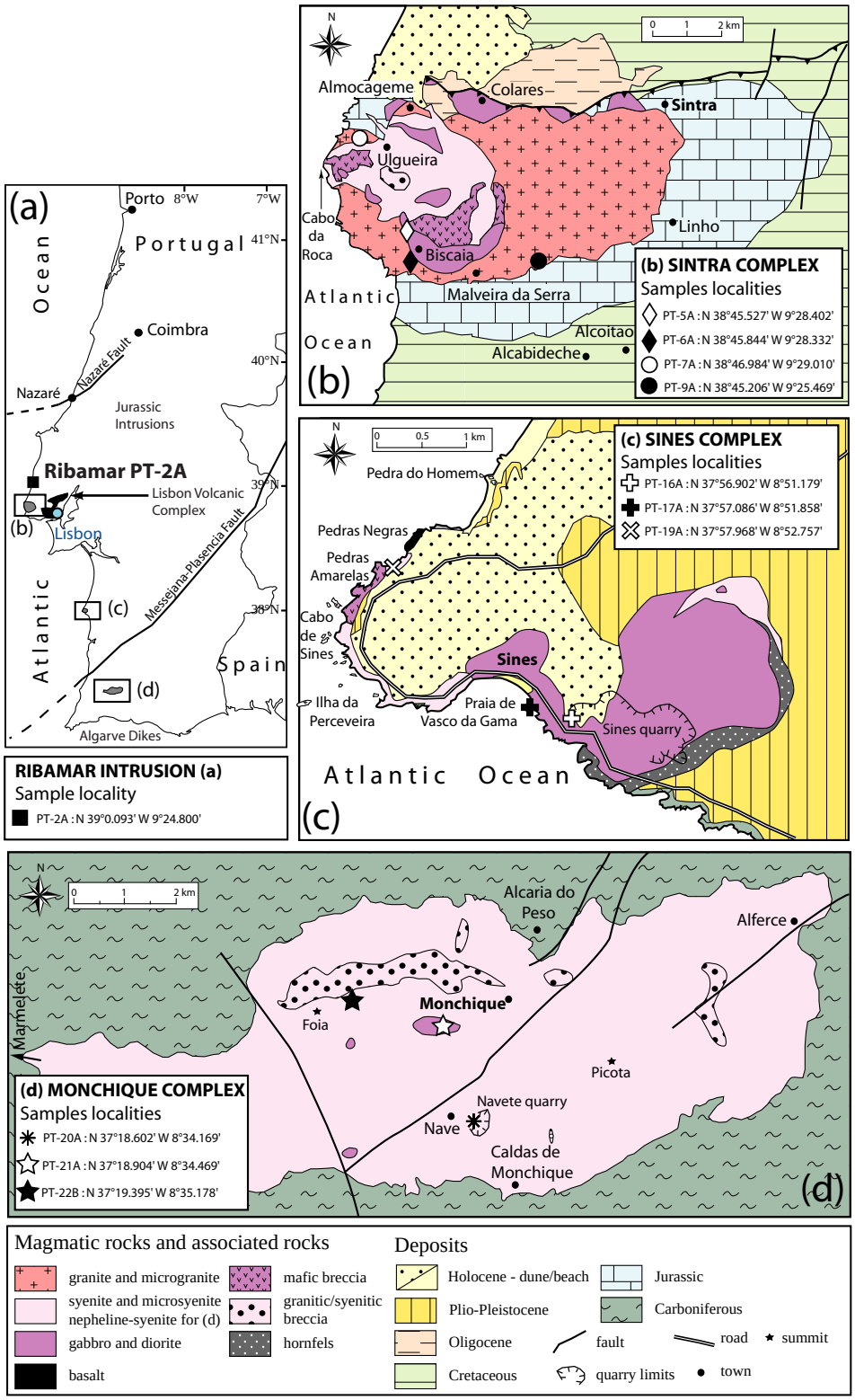
(a)
Porto
8°W
7°W
Portugal
41°N
Ocean
Coimbra
40°N
Nazaré
Nazaré Fault
Jurassic
Intrusions
Ribamar PT-2A
Lisbon Volcanic
Complex
(b)
Lisbon
39°N
Messejana-Plasencia Fault
Atlantic
(c)
38°N
Spain
(d)
Algarve Dikes
RIBAMAR INTRUSION (a)
Sample locality
PT-2A : N 39°0.093' W 9°24.800'
N
0 1 2 km
Almocageme
Colares
Sintra
Ulgueira
Cabo
da
Roca
Linho
Biscaia
Atlantic
Ocean
Malveira da Serra
Alcoitao
Alcabideche
(b)
(b) SINTRA COMPLEX
Samples localities
PT-5A : N 38°45.527' W 9°28.402'
PT-6A : N 38°45.844' W 9°28.332'
PT-7A : N 38°46.984' W 9°29.010'
PT-9A : N 38°45.206' W 9°25.469'
N
0 0.5 1 km
Pedra do Homem
(c) SINES COMPLEX
Samples localities
PT-16A : N 37°56.902' W 8°51.179'
PT-17A : N 37°57.086' W 8°51.858'
PT-19A : N 37°57.968' W 8°52.757'
Pedras Negras
Pedras
Amarelas
Cabo
de
Sines
Sines
Ilha da
Perceveira
Praia de
Vasco da Gama
Sines quarry
Atlantic Ocean
(c)
N
0 1 2 km
Alcaria do
Peso
Alferce
Marmeleete
Monchique
Foia
Picota
Navete quarry
Nave
Caldas de
Monchique
(d)
(d) MONCHIQUE COMPLEX
Samples localities
PT-20A : N 37°18.602' W 8°34.169'
PT-21A : N 37°18.904' W 8°34.469'
PT-22B : N 37°19.395' W 8°35.178'
Magmatic rocks and associated rocks
granite and microgranite
syenite and microsyenite
nepheline-syenite for (d)
gabbro and diorite
basalt
mafic breccia
granitic/syenitic
breccia
hornfels
Deposits
Holocene - dune/beach
Plio-Pleistocene
Oligocene
Cretaceous
Jurassic
Carboniferous
fault
road
summit
quarry limits
town

Figure 2

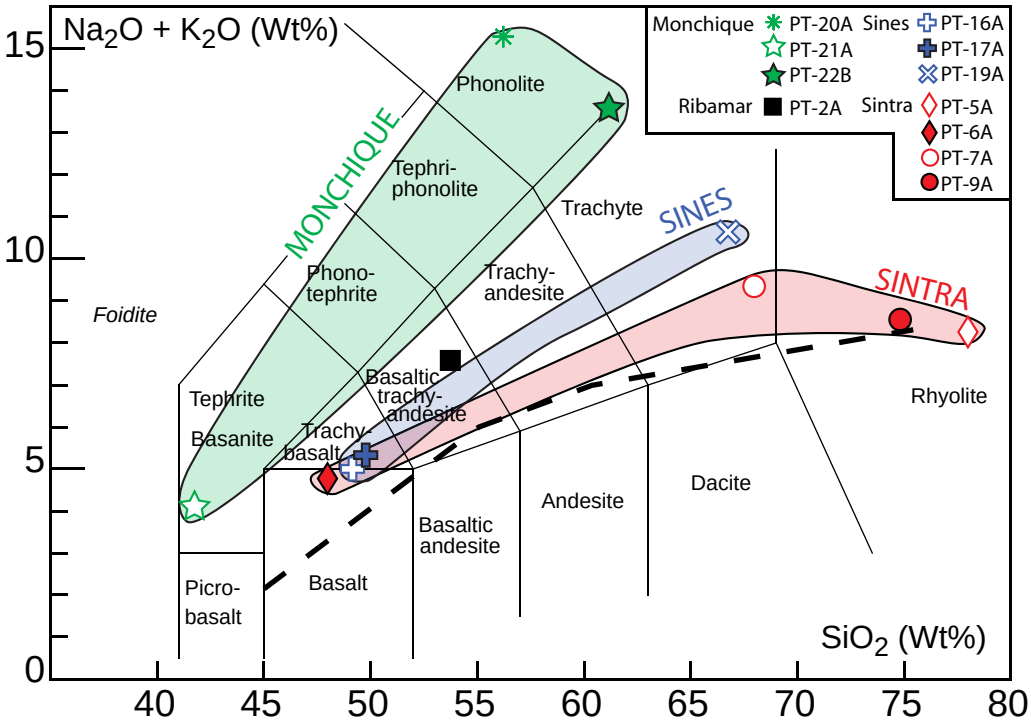
Na2O + K2O (Wt%)
SiO2 (Wt%)
Monchique
PT-20A
PT-21A
PT-22B
Ribamar
PT-2A
Sines
PT-16A
PT-17A
PT-19A
Sintra
PT-5A
PT-6A
PT-7A
PT-9A
MONCHIQUE
SINES
SINTRA
Phonolite
Tephri-phonolite
Trachyte
Phono-tephrite
Trachy-andesite
Foidite
Tephrite
Basanite
Basaltic trachy-andesite
Trachy-basalt
Rhyolite
Dacite
Andesite
Basaltic andesite
Basalt
Picro-basalt
0
5
10
15
40
45
50
55
60
65
70
75
80

Figure 3

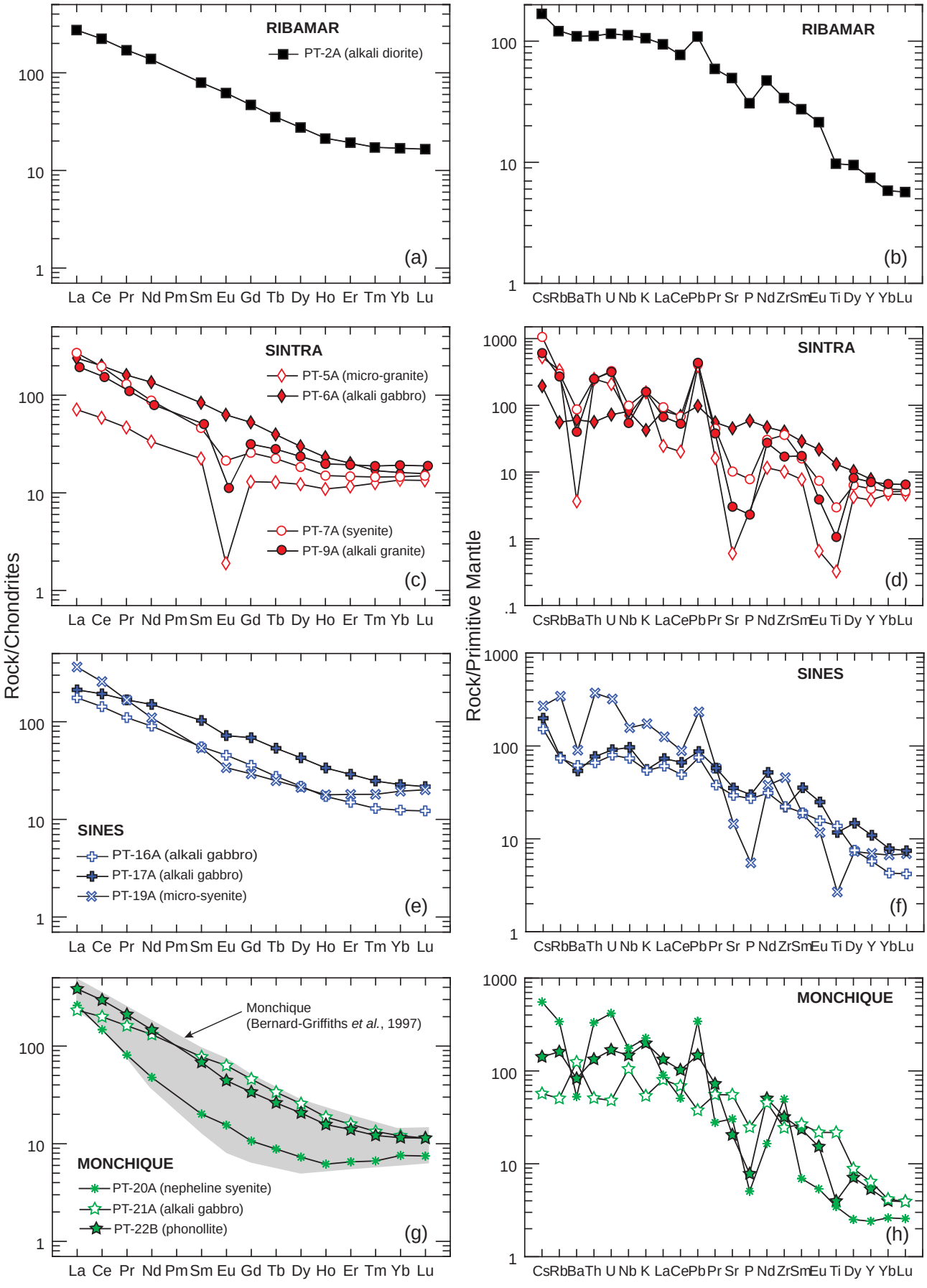
RIBAMAR
PT-2A (alkali diorite)
(a)
(b)
SINTRA
PT-5A (micro-granite)
PT-6A (alkali gabbro)
PT-7A (syenite)
PT-9A (alkali granite)
(c)
(d)
SINES
PT-16A (alkali gabbro)
PT-17A (alkali gabbro)
PT-19A (micro-syenite)
(e)
(f)
Monchique
(Bernard-Griffiths et al., 1997)
MONCHIQUE
PT-20A (nepheline syenite)
PT-21A (alkali gabbro)
PT-22B (phonollite)
(g)
(h)
Rock/Chondrites
Rock/Primitive Mantle
La Ce Pr Nd Pm Sm Eu Gd Tb Dy Ho Er Tm Yb Lu
Cs Rb Ba Th U Nb K La Ce Pb Pr Sr P Nd Zr Sm Eu Ti Dy Y Yb Lu

Figure 4

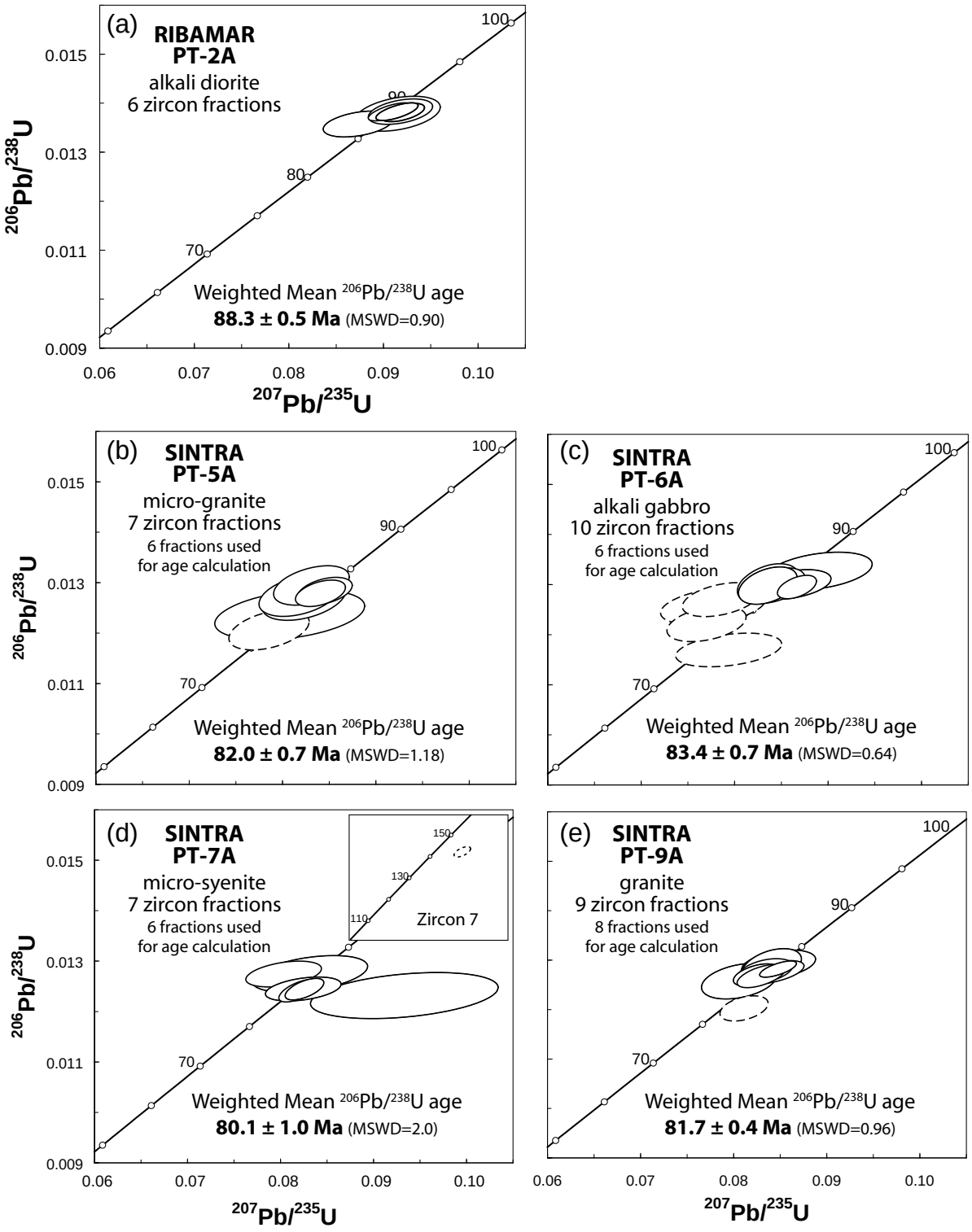
(a)
RIBAMAR
PT-2A
alkali diorite
6 zircon fractions
Weighted Mean 206Pb/238U age
88.3 ± 0.5 Ma (MSWD=0.90)
(b)
SINTRA
PT-5A
micro-granite
7 zircon fractions
6 fractions used
for age calculation
Weighted Mean 206Pb/238U age
82.0 ± 0.7 Ma (MSWD=1.18)
(c)
SINTRA
PT-6A
alkali gabbro
10 zircon fractions
6 fractions used
for age calculation
Weighted Mean 206Pb/238U age
83.4 ± 0.7 Ma (MSWD=0.64)
(d)
SINTRA
PT-7A
micro-syenite
7 zircon fractions
6 fractions used
for age calculation
Zircon 7
Weighted Mean 206Pb/238U age
80.1 ± 1.0 Ma (MSWD=2.0)
(e)
SINTRA
PT-9A
granite
9 zircon fractions
8 fractions used
for age calculation
Weighted Mean 206Pb/238U age
81.7 ± 0.4 Ma (MSWD=0.96)
206Pb/238U
207Pb/235U

Figure 5

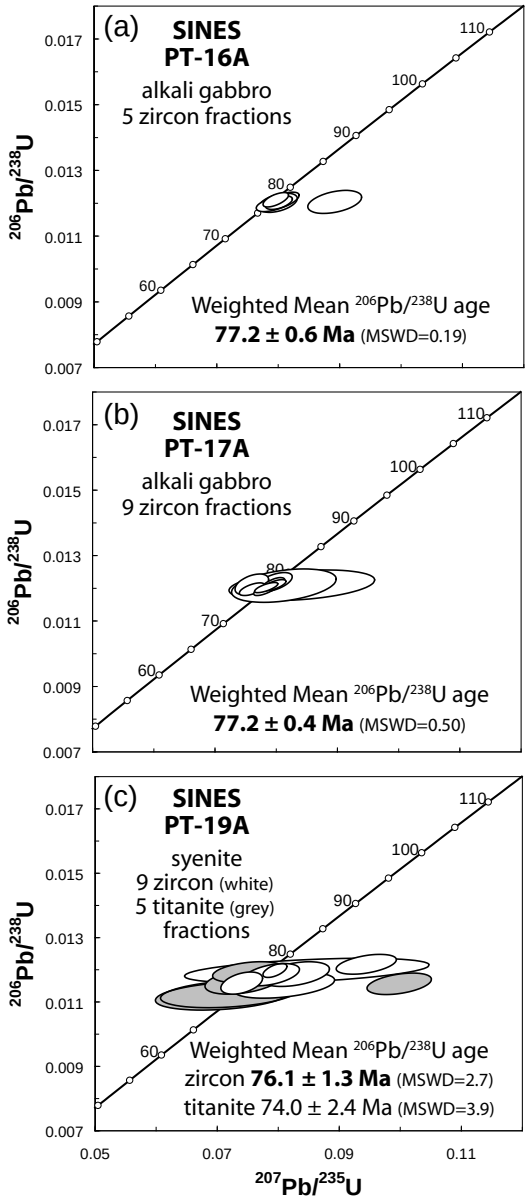
(a)
SINES
PT-16A
alkali gabbro
5 zircon fractions
Weighted Mean 206Pb/238U age
77.2 ± 0.6 Ma (MSWD=0.19)
(b)
SINES
PT-17A
alkali gabbro
9 zircon fractions
Weighted Mean 206Pb/238U age
77.2 ± 0.4 Ma (MSWD=0.50)
(c)
SINES
PT-19A
syenite
9 zircon (white)
5 titanite (grey)
fractions
Weighted Mean 206Pb/238U age
zircon 76.1 ± 1.3 Ma (MSWD=2.7)
titanite 74.0 ± 2.4 Ma (MSWD=3.9)
206Pb/238U
207Pb/235U
0.007
0.009
0.011
0.013
0.015
0.017
0.05
0.07
0.09
0.11
60
70
80
90
100
110

Figure 6

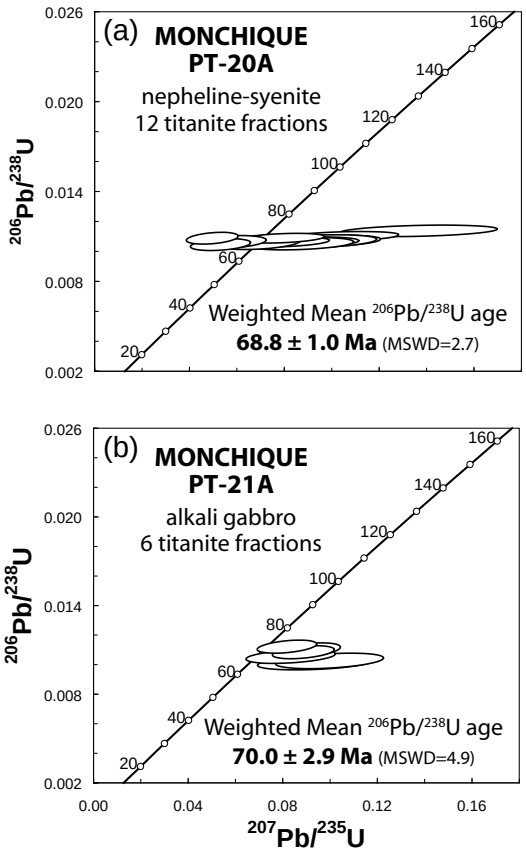
(a)
MONCHIQUE
PT-20A
nepheline-syenite
12 titanite fractions
Weighted Mean 206Pb/238U age
68.8 ± 1.0 Ma (MSWD=2.7)
(b)
MONCHIQUE
PT-21A
alkali gabbro
6 titanite fractions
Weighted Mean 206Pb/238U age
70.0 ± 2.9 Ma (MSWD=4.9)
206Pb/238U
207Pb/235U
0.026
0.020
0.014
0.008
0.002
0.00
0.04
0.08
0.12
0.16
20
40
60
80
100
120
140
160

Figure 7

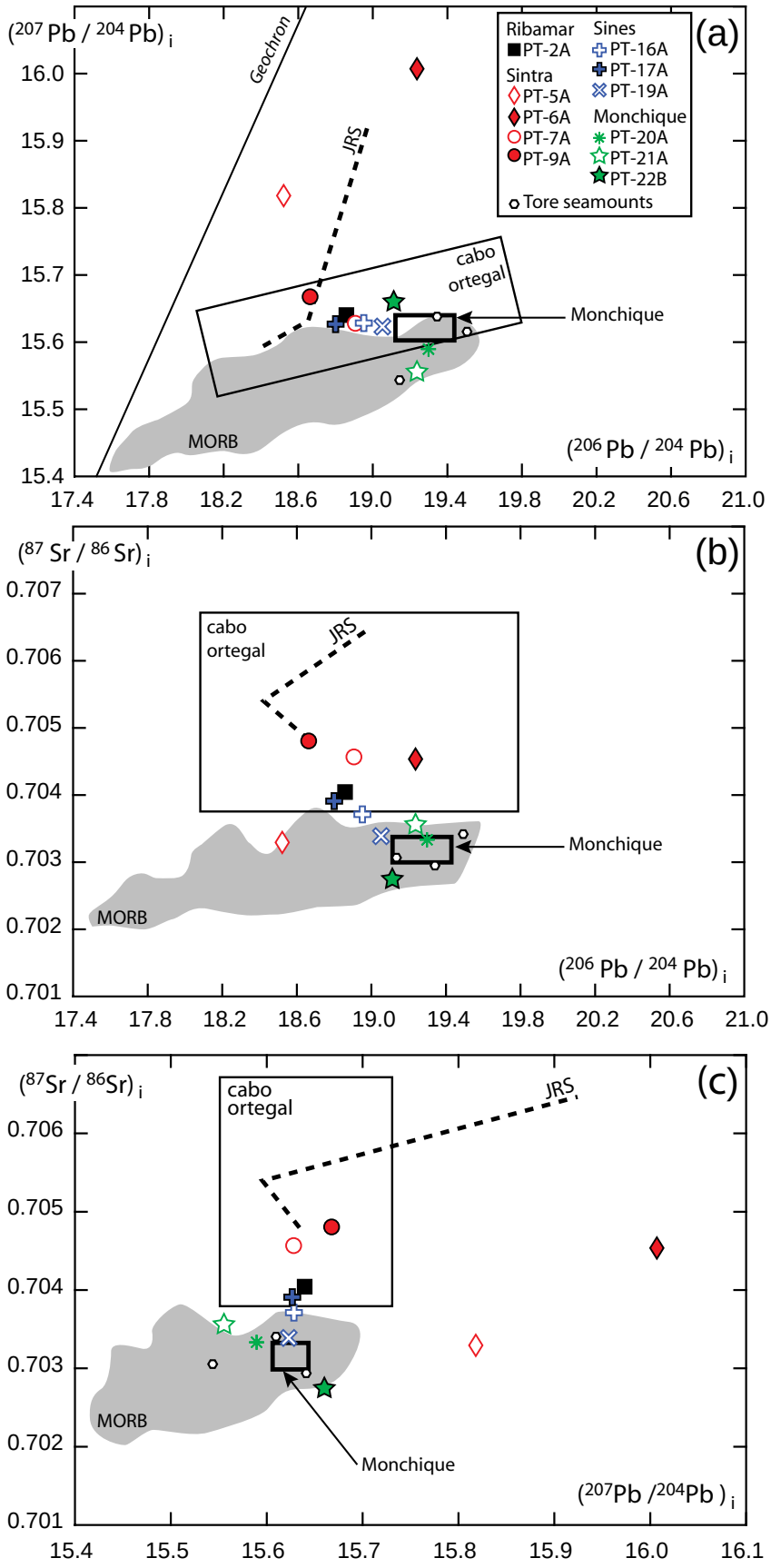
(a)
(207 Pb / 204 Pb) i
Geochron
JRS
cabo ortegal
Monchique
MORB
(206 Pb / 204 Pb) i
Ribamar
PT-2A
Sintra
PT-5A
PT-6A
PT-7A
PT-9A
Sines
PT-16A
PT-17A
PT-19A
Monchique
PT-20A
PT-21A
PT-22B
Tore seamounts
16.0
15.9
15.8
15.7
15.6
15.5
15.4
17.4
17.8
18.2
18.6
19.0
19.4
19.8
20.2
20.6
21.0
(b)
(87 Sr / 86 Sr) i
cabo ortegal
JRS
Monchique
MORB
(206 Pb / 204 Pb) i
0.707
0.706
0.705
0.704
0.703
0.702
0.701
(c)
(87Sr / 86Sr) i
cabo ortegal
JRS
MORB
Monchique
(207Pb /204Pb) i
15.4
15.5
15.6
15.7
15.8
15.9
16.0
16.1

Figure 8

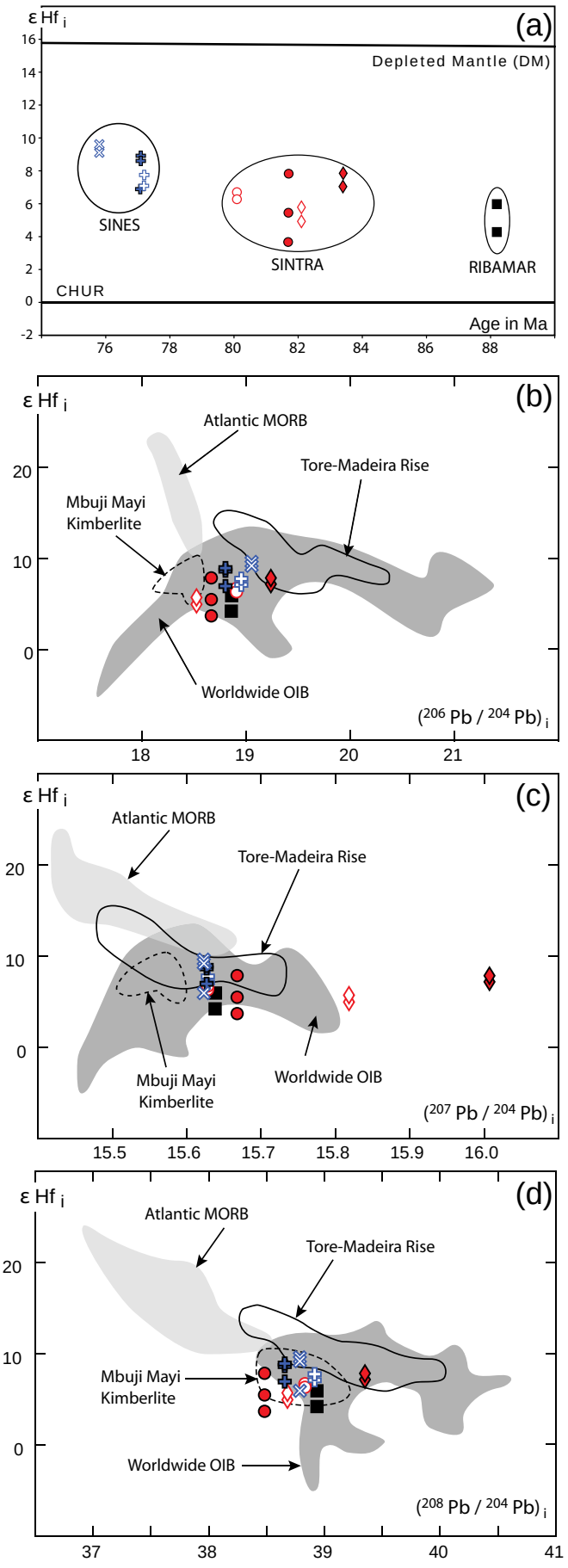
(a)
ε Hf i
Depleted Mantle (DM)
SINES
SINTRA
RIBAMAR
CHUR
Age in Ma
(b)
Atlantic MORB
Tore-Madeira Rise
Mbuji Mayi Kimberlite
Worldwide OIB
(206 Pb / 204 Pb) i
(c)
Atlantic MORB
Tore-Madeira Rise
Mbuji Mayi Kimberlite
Worldwide OIB
(207 Pb / 204 Pb) i
(d)
Atlantic MORB
Tore-Madeira Rise
Mbuji Mayi Kimberlite
Worldwide OIB
(208 Pb / 204 Pb) i

Figure 9

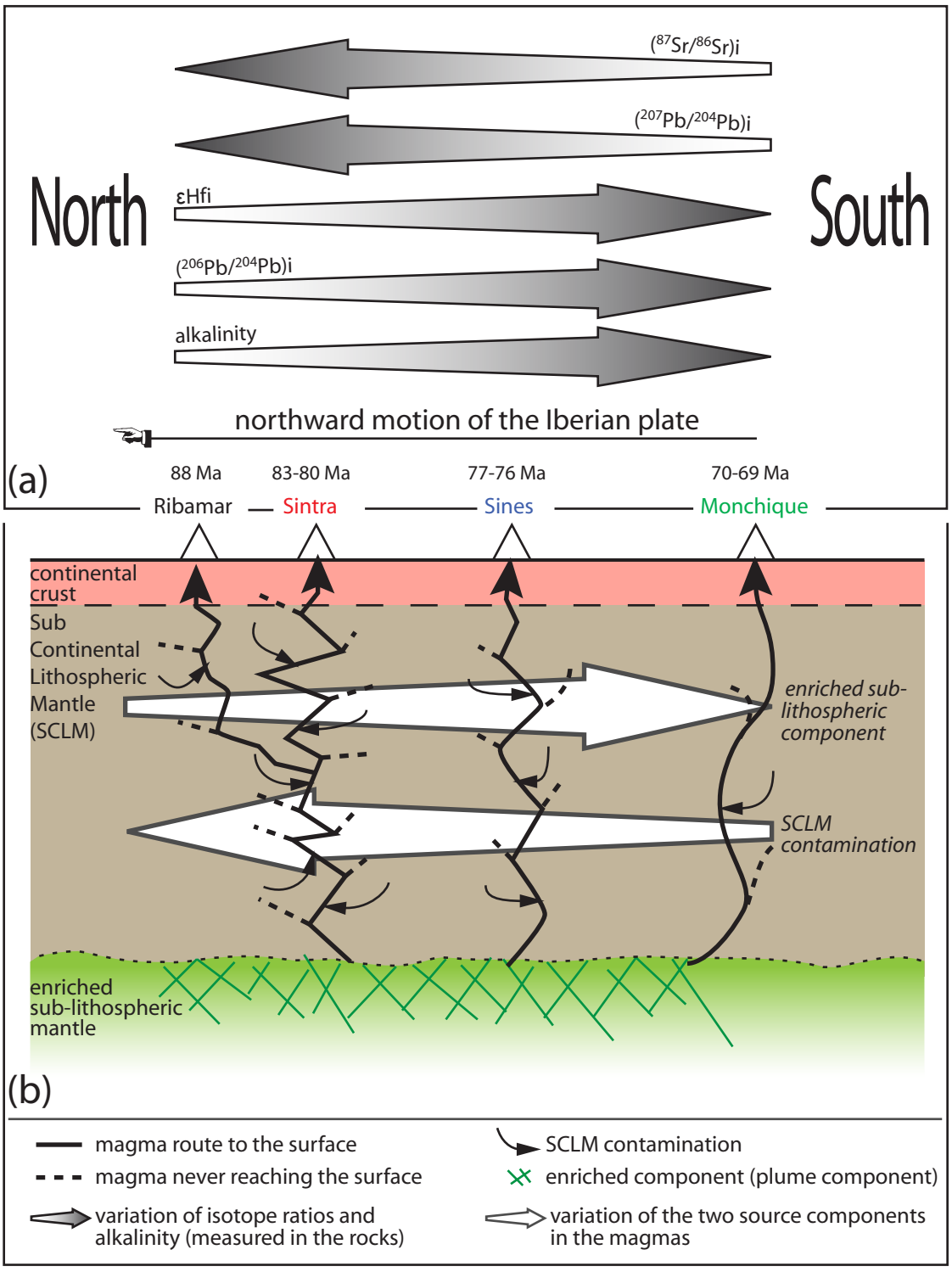
(87Sr/86Sr)i
(207Pb/204Pb)i
North
εHfi
South
(206Pb/204Pb)i
alkalinity
northward motion of the Iberian plate
(a)
88 Ma
83-80 Ma
77-76 Ma
70-69 Ma
Ribamar
Sintra
Sines
Monchique
continental crust
Sub Continental Lithospheric Mantle (SCLM)
enriched sub-lithospheric component
SCLM contamination
enriched sub-lithospheric mantle
(b)
magma route to the surface
magma never reaching the surface
variation of isotope ratios and alkalinity (measured in the rocks)
SCLM contamination
enriched component (plume component)
variation of the two source components in the magmas

Figure 10